UNIVERSITY OF OKLAHOMA

GRADUATE COLLEGE

RELATIONSHIPS BETWEEN LIDAR AEROSOL EXTINCTION AND

BACKSCATTER COEFFICIENTS WITH CCN NUMBER CONCENTRATIONS

IN THE SOUTHEAST ATLANTIC

A THESIS

SUBMITTED TO THE GRADUATE FACULTY

in partial fulfillment of the requirements for the

Degree of

MASTER OF SCIENCE IN METEOROLOGY

By

Emily Lenhardt
Norman, Oklahoma
2021

RELATIONSHIPS BETWEEN LIDAR AEROSOL EXTINCTION AND
BACKSCATTER COEFFICIENTS WITH CCN NUMBER CONCENTRATIONS
IN THE SOUTHEAST ATLANTIC

A THESIS APPROVED FOR THE
SCHOOL OF METEOROLOGY

BY THE COMMITTEE CONSISTING OF

Dr. Jens Redemann, Chair

Dr. Feng Xu

Dr. Cameron Homeyer

Dr. Lan Gao

Acknowledgments

It is truly astonishing how many people have supported the past two years behind this project in large and small ways. Although not in-person for most of that time, I am incredibly thankful for all the support that has made graduate school during a global pandemic possible.

I would like to first thank my advisor, Dr. Jens Redemann, for taking a chance on me two years ago when I had no real research direction or any idea what I was doing, and for being incredibly supportive during not only each step of this project but also during the past two years of graduate courses. I would also like to acknowledge Dr. Lan Gao, for always being available to answer my many questions, for his incredible patience in helping me work through endless MATLAB issues, and for teaching me what thorough research really looks like. To the rest of the CL^{2}EAR group, thank you for your feedback and consistent encouragement at group meetings. I would also like to acknowledge my committee members, Dr. Feng Xu and Dr. Cameron Homeyer, for their support and feedback and willingness to take time to read drafts of this thesis.

I want to thank my family for their support – both from 8 hours away as well as during my time at home presenting at online conferences in my childhood bedroom. I also need to acknowledge my roommate and other School of Meteorology friends, without whom I would have laughed a lot less and felt a lot more lost over the past two years.

I have been truly blessed with this amazing support system, and can only hope to give back what they have given me moving into the future.

Table of Contents

List Of Tables

List Of Figures

Abstract

Due to seasonal biomass burning and the presence of a semi-permanent stratocumulus deck off the western coast of Africa, the Southeast Atlantic (SEA) region is particularly important in terms of characterizing aerosol and cloud impacts on radiative forcing and regional climate. Aerosols that can activate to become cloud droplets, termed cloud condensation nuclei (CCN), provide the direct microphysical link that drive aerosol-cloud interactions. In this study, we examine the relationship between NASA Langley's airborne High Spectral Resolution Lidar 2 (HSRL-2) measurements of backscatter (BSC) and extinction (EXT) coefficients with in situ measured CCN number concentrations obtained during three flight campaigns in the ObseRvations of Aerosols above CLouds and their intEractionS (ORACLES) project. The primary goal of these relationships is development of a method to infer CCN concentrations using remote sensing measurements.

An important precursory step is spatial and temporal collocation of the two data sets, for which sensitivity testing suggests that time windows shorter than 40 minutes and horizontal distances on the order of 2 km are ideal. Results further suggest that the correlation between HSRL-2 BSC/EXT and in-situ CCN is strongest for "dry" conditions, with ambient relative humidity less than 40-50%. The three flight campaigns demonstrate important similarities in the BSC/EXT – CCN relationship, pointing to fundamental similarities in biomass burning aerosol (BBA) microphysics. Additionally, aerosol microphysical properties, e.g., size distribution and independently derived refractive indices, are used to compare theoretically calculated

backscatter and extinction to results found using HSRL-2 measurements. Ultimately this information will be useful when developing methods for constraining CCN concentrations with lidar measurements alone for locations where in-situ data are not available, specifically over the SEA. This will aid in constraining radiative effects specifically of BBA, and the methodology will serve as a starting point for future related studies on different aerosol types.

Chapter 1

Background

1.1   Background on Atmospheric Aerosols

One of the most important environmental questions moving into the future is how Earth's climate will respond to anthropogenic emissions and different radiative forcings over time. Atmospheric aerosols, both natural and anthropogenic, play an important role in terms of climate uncertainty and global warming. Anthropogenic aerosols are of specific interest as, left unchecked, their emissions will continue to increase over time. Therefore, understanding the impacts of aerosols on our environment is a pertinent issue (of the IPCC 2013).

In a review on aerosols, climate, and the hydrological cycle by Ramanathan (2001), atmospheric aerosols generally comprise four broad groups that include sulfates, carbonaceous aerosols, dust, and sea salt. Of all atmospheric aerosols, anthropogenically sourced and natural aerosols have been found to contribute almost equally to global aerosol optical depth (AOD; Ramanathan 2001). Due to their short lifetimes, atmospheric aerosols do not play a significant role in global trends of AOD but are more influential to AOD on regional scales (Buchholz et al. 2021). While greenhouse gases can result in warming due to interaction with outgoing longwave radiation, aerosols primarily interact with incoming solar shortwave radiation either directly or

indirectly (Haywood and Boucher 2000; Lohmann and Feichter 2005; Ramanathan 2001), as described in the following section. Currently, the overall impact of aerosols is reported to be contributing to global cooling, offsetting significant warming caused by greenhouse gases (of the IPCC 2013).

1.2   Aerosol Direct and Indirect Effects

Aerosol direct effects include interactions between aerosols and radiation through particle absorption and scattering. Atmospheric aerosols typically have a size range of 0.1 to a few microns and reside in the Mie scattering regime, which causes mostly forward scattering of light while a small fraction is scattered backwards (Budyko 1969; Mitchell 1971). Incoming solar shortwave radiation scattered backwards to space causes a net loss of energy in the Earth system. This effect, on its own, results in lowered equilibrium temperature at Earth's surface, but depending on composition, aerosols can absorb solar radiation at the same time, causing a warming effect (Boucher et al. 2013; Lohmann and Feichter 2005; Mitchell 1971; Prather et al. 2008; Ramanathan 2001). Although there have been significant efforts to quantify aerosol direct radiative effects, there is much room for future improvement. This includes realistic representations of aerosol microphysics and optical properties from multi-instruments (e.g., active/passive remote sensors in space) and ensemble models, as well as estimating the all-sky direct effect considering aerosol and cloud diurnal variations.

Aerosol indirect effects are defined by the way aerosols interact with clouds, and consequently, how those clouds interact with radiation (e.g., cloud albedo effect).

This is an important consideration in terms of future climate, as clouds contribute more to total reflection of solar radiation than aerosols alone (Twomey 1974). It is also important due to our poor current understanding of how the aerosol indirect effect mediates climate forcing (Myrhe et al. 2013).

As aerosol concentration increases, cloud droplet concentration will increase and cloud droplet effective radius will decrease, assuming a constant liquid water content (Figure 1.1). This well-known process, known as the Twomey effect or aerosol first indirect effect, can increase cloud albedo, or the fraction of incident light energy reflected by a cloud that does not reach earth's surface or the below-cloud atmosphere (Twomey 1974). Although the corresponding increase in cloud albedo may be small for a small change in droplet concentration or optical thickness, resulting changes in incoming solar energy can be incredibly impactful in terms of resultant temperature differences (Andreae 2009; Budyko 1969; Twomey 1974).

The second aerosol indirect effect, or the Albrecht effect, describes how aerosols influence cloud lifetime, and resultantly, how increased cloud lifetime alters potential effects of incoming solar radiation interacting with clouds. Albrecht (1989) argued that drizzle occurs more frequently in marine stratocumulus clouds when droplet concentration decreases. Therefore, increased aerosol (and droplet) concentration in oceanic regions causes reductions in drizzle, subsequent reductions in aerosol removal, and prolonged cloud lifetime. The most recent Intergovernmental Panel on Climate Change (IPCC) report found that when climate models include this second indirect effect overall indirect aerosol radiative forcing increases by a factor of 1.25 to over a factor of 2 (Penner et al. 2001).

Aerosol-cloud interactions

(a)

Aerosols serve as cloud condensation nuclei upon which liquid droplets can form.

(b)

More aerosols result in a larger concentration of smaller droplets, leading to a brighter cloud. However there are many other possible aerosol–cloud–precipitation processes which may amplify or dampen this effect.
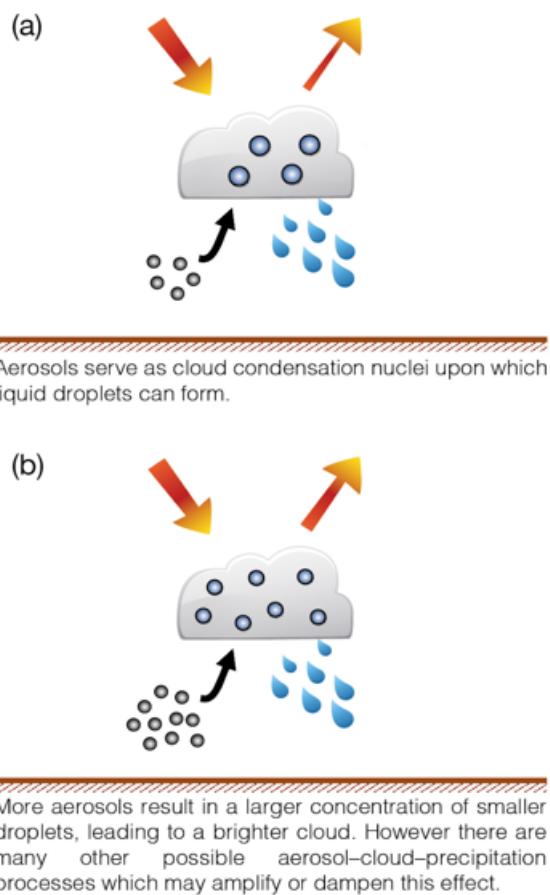
Figure 1.1: Graphic from Chapter 7 of the 2013 IPCC reports (Boucher et al. 2013) depicts overview of aerosol-cloud interactions with a) clean and b) polluted low-level clouds.

1.3 Aerosol-Cloud Interactions and CCN

Aerosol-cloud interactions have high uncertainty because of poor understanding of basic processes involved. Fundamental understanding is complicated due to, in short, the multiple ways that aerosols can impact cloud processes and clouds, in return, can modify aerosols (Boucher et al. 2013). In addition, the radiative and microphysical effects of aerosols on clouds are correlated and often dependent on one another at

large scales (Andreae 2009). A few factors complicating observations of aerosol-cloud interactions include limited ability of satellites (e.g., MODIS) to distinguish between cloud and aerosol properties simultaneously, as well as the issue of aerosols swelling due to high relative humidity in the vicinity of clouds. This swelling can artificially increase aerosol optical properties without a corresponding increase in aerosol concentration. Furthermore, observational scale and meteorological context can buffer the responses of clouds to aerosol perturbations, complicating the study (Rosenfeld et al. 2014; Stevens and Feingold 2009). A lack of fundamental understanding of how exactly these processes work then causes misrepresentation in large-scale models (Boucher et al. 2013). Furthermore, modelling requires additional information about aerosol number concentration, chemical composition of aerosols, and vertical velocity on a cloud scale, which vary for different parts of the globe and often are not well-characterized (Lohmann and Feichter 2005).

Due to the challenges of fully understanding aerosol-cloud interaction processes and capturing them in models, the global impact that aerosols have on Earth's climate is highly uncertain. Numerous agents of radiative forcing of climate have been defined by the IPCC, but the one estimated to have the highest uncertainty is aerosol-cloud interactions. According to the 2013 IPCC report, as shown in Figure 1.2, aerosol-cloud interactions may have a large cooling effect on climate, but to an extent which is highly uncertain (Myrhe et al. 2013). For example, in a recent study by Bellouin et al. (2020) using Copernicus Atmosphere Monitoring Service (CAMS) reanalysis data, results suggested that aerosol-cloud interactions globally averaged between 2003-2017

contributed approximately -0.69 W m^{-2}, a large fraction relative to total aerosol radiative forcing averaging about -1.25 W m^{-2}.
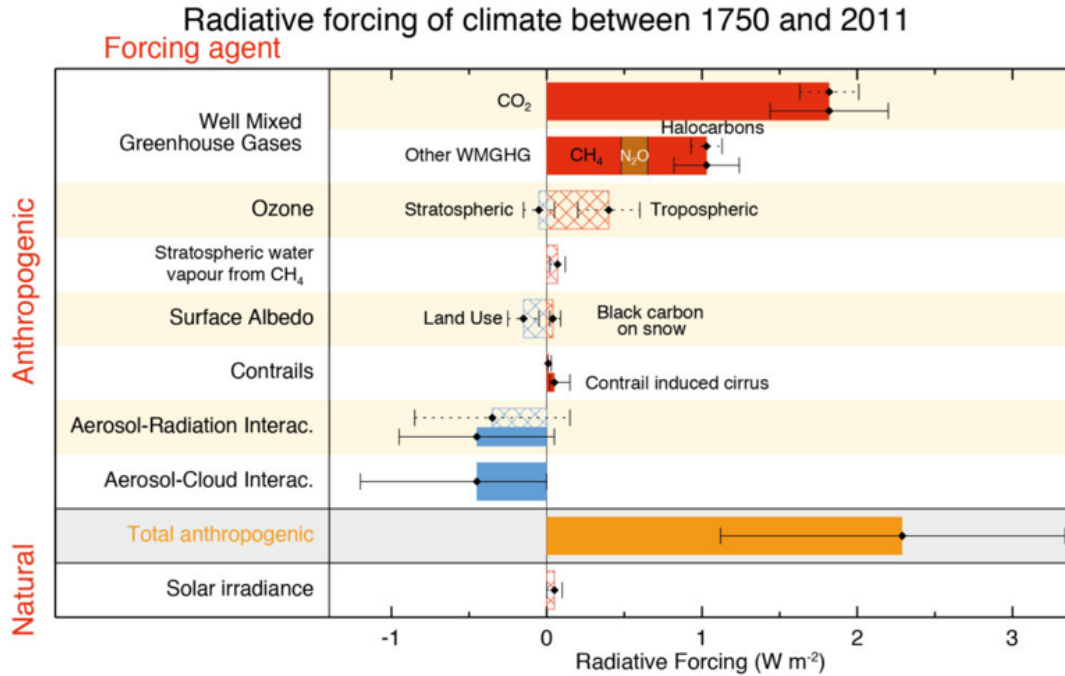
Figure 1.2: Graphic from Chapter 8 of the 2013 IPCC reports (Myrhe et al. 2013) shows radiative forcing (hatched), effective radiative forcing (solid), and uncertainties for various natural and anthropogenic forcings of climate between 1750-2011.

To model and predict future climate change, one key component to better understand is aerosol-cloud interactions to reduce uncertainty in how they impact climate. An important first step toward this goal is accurate representation of aerosols that can affect clouds. Cloud condensation nuclei (CCN) are the aerosols onto which water vapor condenses to form cloud droplets, making them a key component of this area of study (Andreae and Rosenfeld 2008). CCN are distinct within the realm of atmospheric aerosols as not all aerosols are able to facilitate cloud droplet formation.

Rather, nucleation is a function of aerosol size and chemical composition, as well as ambient supersaturation (Andreae and Rosenfeld 2008).

1.4   Köhler Theory

An important theory defining cloud droplet nucleation is Köhler Theory, which states that dry, soluble aerosols have a specific critical supersaturation corresponding to a critical radius, depending on their chemical compositions. Once a drop grows slightly larger than its critical radius, spontaneous growth will occur until it becomes a cloud droplet (Andreae and Rosenfeld 2008; Köhler 1936). Particles that do nucleate into cloud droplets via this process are called CCN. Köhler Theory can be used to calculate theoretical CCN concentration values and model CCN activity of atmospheric aerosols.

Closure studies to improve predictions of aerosol-cloud interactions have been done using aerosol size distribution and chemical composition information as inputs to the Köhler equations (Sotiropoulou et al. 2007). Adaptations of Köhler Theory, such as that by Petters and Kreidenweis (2007), have also been developed. Their version is called κ-Köhler Theory, where κ is a hygroscopicity parameter dependent on aerosol characteristics in a certain region. This equation is given below (Eqn. 1.1), where D is the diameter of the droplet, D_d is the dry diameter, κ is the hygroscopicity parameter, $\sigma_{s/a}$ is the surface tension of a solution/air interface, M_w is the molecular weight of water, R is the universal gas constant, T is temperature, and ρ_w is the density of

water (Petters and Kreidenweis 2007). Solving this equation gives saturation ratio (S) as a function of droplet size and hygroscopicity.

$$S(D) = \frac{D^3 - D_d^3}{D^3 - D_d^3(1 - \kappa)} exp \frac{4\sigma_{s/a} M_w}{RT\rho_w D} \tag{1.1}$$

1.5   In Situ and Remote Sensing of CCN

While Köhler Theory provides a means to improve predictions of aerosol-cloud interactions via theoretical calculations, in situ CCN measurements are critical. Previous field studies that have focused on measuring aerosols through in situ instruments have used ground-based sites, aircraft, balloons, ships, and unmanned aerial vehicles. However, field observations are limited to a small spatial and temporal scale (Prather et al. 2008). Since aerosols impact radiative forcing globally, we need another way to obtain information about their concentrations and characteristics at larger scales. Satellite and airborne remote sensing measurements can provide reliable constraints on global aerosol distributions and are also beneficial considering the high spatial and temporal variability of aerosols (Ramanathan 2001). Furthermore, when combined with models, satellite measurements are useful for extrapolating findings to a larger scale than can be explored using in situ methods (Prather et al. 2008).

Numerous studies have used satellite and remote sensing techniques to glean information about aerosol optical properties in various regions of interest (Ghan and Collins 2004; Kapustin et al. 2006; Kaufman et al. 2003; Liu et al. 2007; Lv et al.

2018; Shinozuka et al. 2009), and while there are significant benefits to these techniques, there are also limitations. For example, complications with retrieving CCN information often stem from a lack of supplemental information. Since aerosol chemical composition impacts the ability of aerosols to activate as CCN, retrievals of CCN concentration from satellite measurements could be improved with information about regional chemical composition (Kapustin et al. 2006; Shinozuka et al. 2009). Another common issue is hygroscopicity. Highly hygroscopic aerosols tend to swell under high relative humidities, which can increase satellite retrieved aerosol optical properties without a corresponding increase in aerosol and/or CCN number concentration. Therefore, information about aerosol hygroscopicity and relative humidity can improve CCN retrievals from satellite measurements (Jeong et al. 2007; Kapustin et al. 2006; Liu et al. 2007; Shinozuka et al. 2009).

In addition to these complications, other limitations lie in instrument capabilities. More specifically, passive remote sensing instruments (e.g., polarimeter, radiometer) measure optical properties for entire columns of the atmosphere, and for all present aerosols. While aerosols of various sizes all contribute to measured optics, those that act as CCN usually only represent the smallest portion of the size distribution. Therefore, it is challenging to get independent information about CCN, and understanding vertical distributions is also incredibly difficult. Ghan et al. (2006) used lidar extinction and backscatter, among other measurements, to retrieve CCN profiles, and vertical heterogeneity of aerosol size distribution and composition was found to be the dominant source of error in the subsequent CCN retrieval.

Similarly, a study by Lv et al. (2018) developed a retrieval method to estimate CCN concentration using extinction and backscatter from multiwavelength lidar systems such as HSRL. In a case study at the U.S. Department of Energy's Atmospheric Radiation Measurement Climate Research Facility Southern Great Plains (SGP) site, CCN concentrations derived from the lidar retrieval method were well correlated with ground-based in situ measurements (Figure 1.3). However, one issue in this case was vertical heterogeneity of the atmosphere during different time periods. Another example of an issue with distinguishing CCN was seen in a study by Ghan and Collins (2004) that used ground-based lidars. Here they measured a dust layer that contributed significantly to backscatter and extinction returns but had little effect on CCN concentration. An additional issue can occur due to the size of most CCN. Oftentimes they are too small to contribute significantly to total radiances, meaning that remote sensing measurements may not capture them well (Kapustin et al. 2006).

1.6   Mie Scattering Theory

While remote sensing techniques have been used to glean information about aerosol and CCN concentrations through measured optical properties, the same optical properties can be calculated based on light scattering theory. Spherical particles at a size similar to the wavelength of incident radiation, such as atmospheric aerosols and CCN, fall in the Mie scattering regime. Such particles tend to strongly favor forward scattering, as opposed to smaller molecules in the Raleigh regime (Petty 2006). The resultant extinction and scattering coefficients of particles in the Mie regime can be

calculated using Eqn. 1.2 shown below, where β is the extinction or scattering coefficient, σ is the extinction or scattering cross section, $n(r)dr$ is the particle number frequency distribution, and Q is the extinction or scattering efficiency of a single particle.

$$\beta_{ext/sca} = \int_{r_1}^{r_2} \beta_{ext/sca}(m, r, \lambda) * n(r) \, dr \ = \int_{r_1}^{r_2} \pi r^2 * Q_{ext/sca}(m, r, \lambda) * n(r) \, dr \quad (1.2)$$

Extinction and scattering cross section (β) and efficiency (Q) are both functions of refractive index (m), radius (r), and wavelength (λ) of incident radiation. Refractive index is dependent on aerosol type, as is the size distribution of aerosols. For many aerosol types, a bimodal distribution can be assumed that contains a fine and coarse mode. Such a distribution is given by Eqn. 1.3, where $n(r)$ gives number of particles per volume of a certain size bin, N_0 is total number of particles per unit volume, S is geometric standard deviation, r_m is median radius of the distribution, and r is particle radius. In practice, the sum of two independent lognormal size distributions can be used to represent both the fine and coarse mode of a given aerosol type.

$$n(r) = \frac{N_0}{\sqrt{2\pi}} \frac{1}{ln(S)} \frac{1}{r} exp \left[-\frac{(lnr - lnr_m)^2}{2ln^2(S)} \right] \quad (1.3)$$
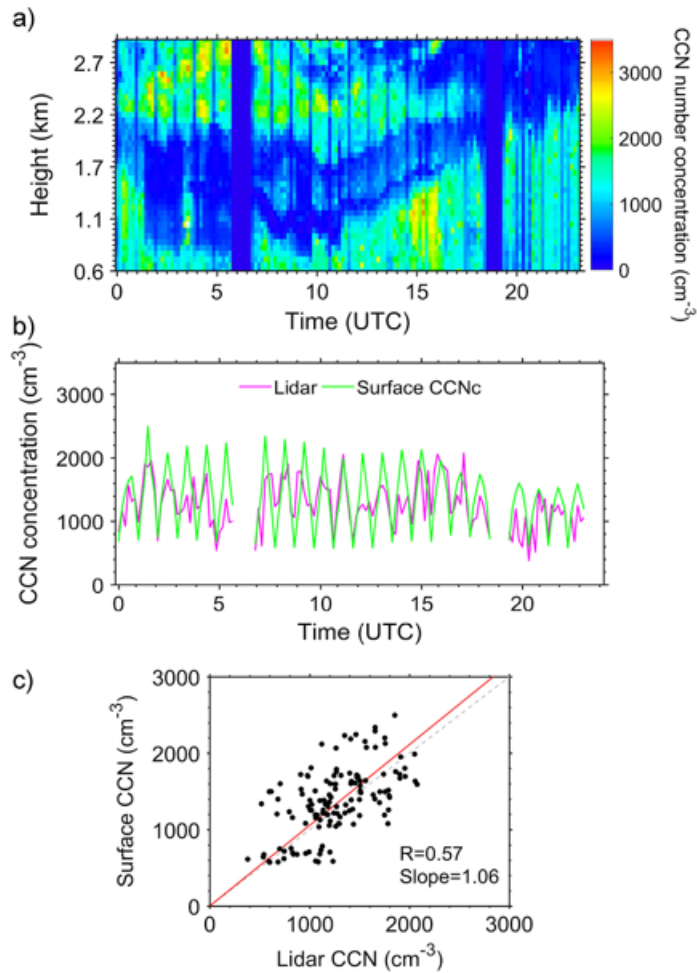
Figure 1.3: Results from a study by Lv et al. (2018) show a) spatiotemporal distributions of retrieved CCN concentrations, b) time series of retrieved (magenta) and surface measured (green) CCN, and c) surface CCN concentration as a function of lidar retrieved CCN concentrations.

Chapter 2

Introduction

2.1 Southeast Atlantic

This study will aim to further our understanding of CCN concentrations over the Southeast Atlantic (SEA). The SEA is of particular interest and importance due to a seasonal cycle from July through October of biomass burning emissions advected westward from southwestern Africa atop a semi-permanent deck of marine stratocumulus clouds. Most of these smoke aerosols are located above and separated from a large stratocumulus deck, but at different times and locations can be entrained into the boundary layer, directly interacting with clouds (Adebiyi et al. 2015; Kaufman et al. 2003; Ross et al. 2003; Zuidema et al. 2016). Stratocumulus clouds are major climate thermostats on a global scale yet remain poorly represented in climate models as being too few in quantity and too bright (Bony and Dufresne 2005; Nam et al. 2012). For this reason, the potential role of CCN is elevated in the SEA.

As alluded to previously, the primary aerosols expected to serve as CCN in this region are biomass burning aerosols (BBA). Although the exact chemical composition of BBA depends on the type of material being burned as well as specific fire conditions, black carbon is often one component emitted that absorbs solar radiation (Andreae and Merlet 2001; Martins et al. 1998). Although not the focus of this study, another

unique aspect of the SEA is the presence of both absorbing BBA and stratocumulus clouds that reflect solar radiation and cause cooling (Lin et al. 2009; Zuidema et al. 2016). While most BBA are located above the stratocumulus deck, the location of some BBA within the boundary layer or of varying distance from the coast may result in different radiative and microphysical effects (Che et al. 2020; Zuidema et al. 2016).

The presence of BBA in the SEA is important for this study due to their high soluble fraction that increases efficiency for activation as CCN (Andreae and Rosenfeld 2008). Che et al. (2020) showed that BBA are the primary source of CCN in the marine stratocumulus deck over the SEA, accounting for about 68% of total CCN at 0.2% supersaturation. Furthermore, in a study over Southern Africa by Ross et al. (2003), a north-south gradient in CCN concentration was found to be present during the burning season, with increased concentrations further north dominated by BBA, while most CCN in the southern region were from anthropogenic and industrial emissions.

2.2   ORACLES Campaign and Dataset

The opportunity to investigate cloud-relevant aerosols using remote sensing and in situ methods over the SEA is provided through the National Aeronautics and Space Administration (NASA) ObseRvations of Aerosols above CLouds and their intEractionS (ORACLES) campaign (Redemann et al. 2021). This investigation occurred from 2016 to 2018 over Southern Africa (Figure 2.1). It focused on filling the observational gap regarding aerosol and cloud properties to improve climate model representation
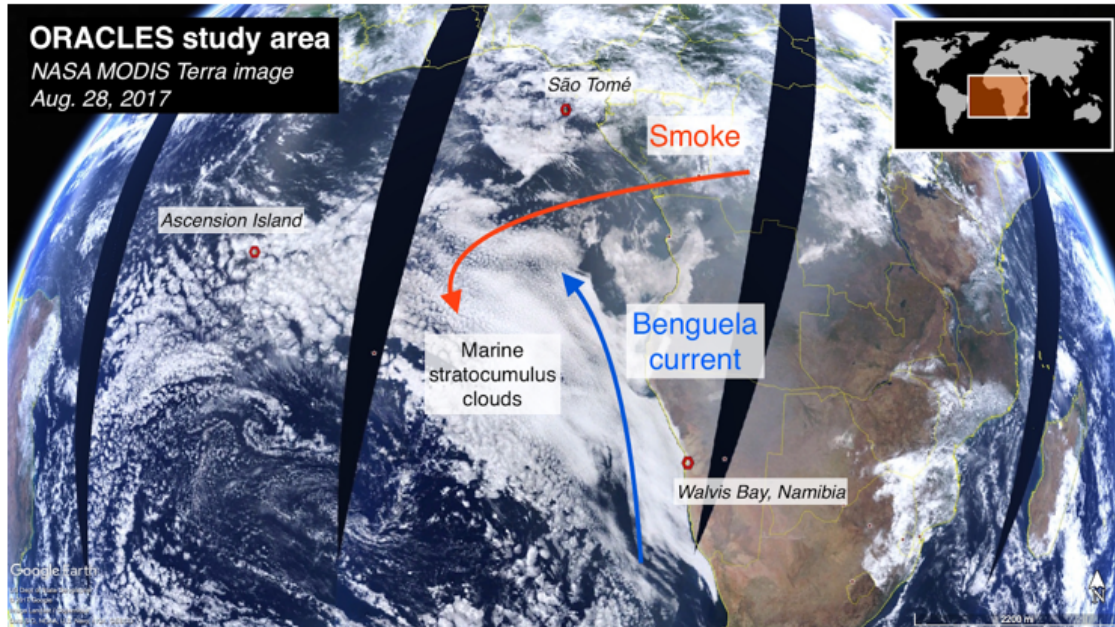
Figure 2.1: Satellite image of the ORACLES study area, featuring the biomass burning smoke plume, semi-permanent marine stratocumulus clouds, and Benguela current.

of aerosol-cloud interactions. These observations were made using a combination of remote sensing and in situ instruments located on the NASA P-3 (2016-2018) and ER-2 (2016 only) aircraft, and deployments were based in Walvis Bay, Namibia in 2016 and São Tomé and Príncipe in 2017 and 2018. Flight tracks for each year and aircraft are shown in Figure 2.2.

A summary of the ORACLES science questions and related objectives are shown in Figure 2.3 (Redemann et al. 2021). Science question 3 (Q3) links aerosol (CCN) and cloud properties, making it most related to this project's focus. Additionally, a major objective of the campaign was to develop a remote sensing testbed for future satellite studies. For example, this project utilizes data from the High Spectral Resolution Lidar 2 (HSRL-2), a 3 wavelength backscatter and 2 wavelength extinction ($3\beta + 2\alpha$) lidar. Use of data from this instrument, as well as additional remote sensing
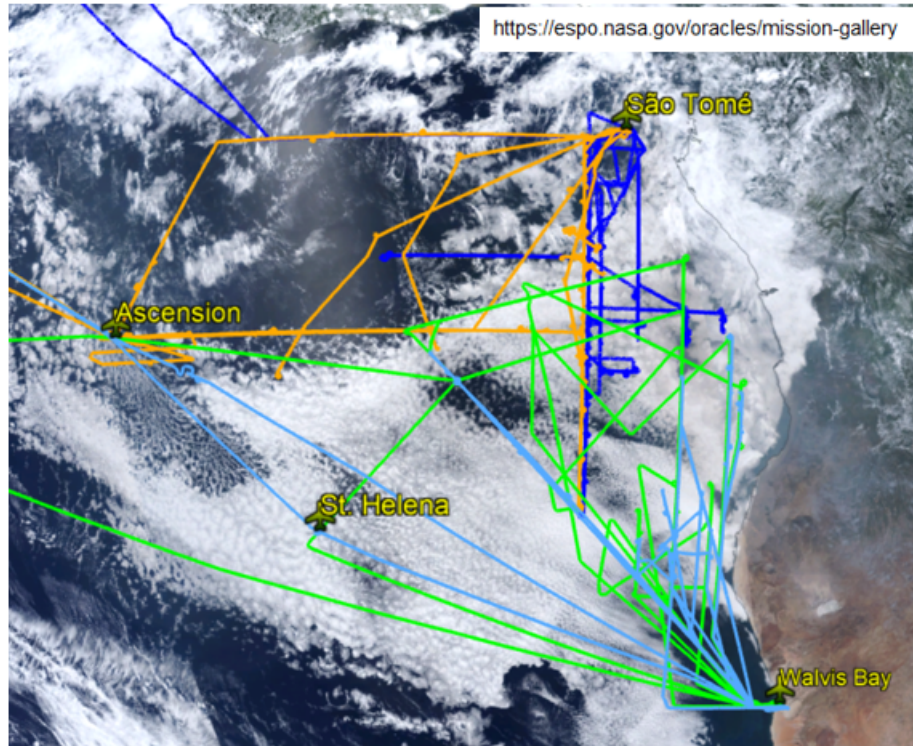
Figure 2.2: Flight tracks over the Southeast Atlantic color-coded by year and aircraft.

instruments and techniques used during ORACLES, will inform the development of new and future satellite deployments.

2.3 Project Goals and Implications

Although there are numerous applications and uses for HSRL-2 capabilities, this project will focus on developing relationships between in situ measured CCN concentrations with HSRL-2 backscatter (BSC) and extinction (EXT) coefficients. The broad goal of these relationships is to be able to predict CCN concentration using

Science questions	Related science objectives
Q1: what is the direct radiative effect of the African biomass burning (BB) aerosol layer in clear- and cloudy-sky conditions over the SE Atlantic?	O1-1 (aerosol spatial evolution): determine the evolution of the BB aerosol microphysical and spectral radiative properties as the aerosol is transported across the South Atlantic. O1-2 (aerosol-induced radiative fluxes): measure aerosol-induced spectral radiative fluxes as a function of cloud albedo and aerosol properties. O1-3 (seasonal aerosol variation): assess the key factors that control the seasonal variation in aerosol direct effects.
Q2: how does absorption of solar radiation by African biomass burning (BB) aerosol change atmospheric stability, circulation, and ultimately cloud properties?	O2-1 (relative vertical distribution): determine the seasonally varying relative vertical distributions of aerosol and cloud properties as a function of distance from shore. O2-2 (aerosol–cloud heating rates): constrain aerosol-induced heating rates for aerosol layers above, within, and below cloud. O2-3 (cloud changes due to aerosol-induced heating): investigate the sensitivity of cloud structure and condensate to aerosol-induced heating rates.
Q3: how do BB aerosols affect cloud droplet size distributions, precipitation, and the persistence of clouds over the SE Atlantic?	O3-1 (mixing survey): survey the location and extent of aerosol mixing into the boundary layer (BL) and its seasonal variation. O3-2 (cloud changes due to aerosol mixing): measure changes in cloud microphysical properties, albedo, and precipitation as a function of aerosol mixing into the BL. O3-3 (cloud changes due to aerosol-suppressed precipitation): investigate the sensitivity of cloud structure and condensate to aerosol-induced suppression in precipitation.

Figure 2.3: Primary and related science objectives for the ORACLES campaign (Redemann et al. 2021). Q3 (boxed in orange) is most directly related to this study's focus on aerosols (CCN) that define aerosol-cloud interactions.

lidar measurements alone, without the need for in situ observations. In situ data sets are valuable but relatively expensive and difficult to obtain at numerous time periods and locations. Conversely, satellite-based lidar observations would be more realistic to obtain on a continuous basis around the globe.

Figure 2.4 provides a visual example of why CCN concentration values derived from lidar coefficients would be valuable. In the background of this image is a Weather Research and Forecasting (WRF) Model curtain of CCN concentration and overlaid (scatter points) are in situ CCN measurements from an ORACLES P-3 track on 12 September 2016. One important initial observation is that the model gives a complete curtain of data that would be unattainable using in situ measurements alone. However, without any in situ values for comparison, there are no adequate means for
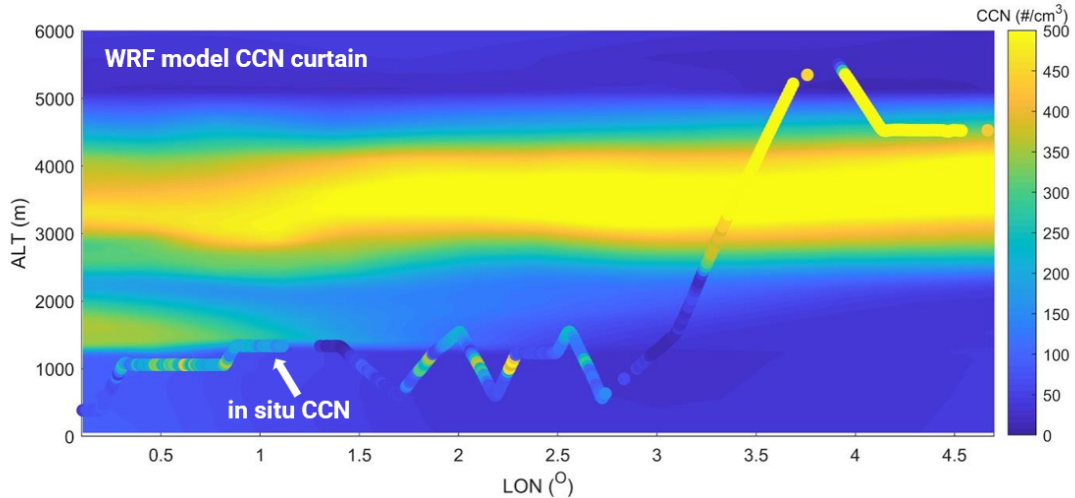
Figure 2.4: WRF curtain of CCN concentration (background, gradient) and overlaid in situ CCN concentration measurements (scatter points) for the corresponding OR-ACLES P-3 track on 12 September 2016 show discrepancies between model output and in situ measured values. Figure provided by Lan Gao, WRF data provided by Pablo Saide & Team at UCLA.

assessment of model reliability. For example, available in situ measurements allow us to see that in this case the WRF data underestimates CCN concentrations at low altitudes as well as the extent of the smoke plume aloft, as seen in the 3000-4500 m layer. On the other hand, while this in situ CCN concentration data is extremely valuable, it only covers a small portion of the vertical domain.

Understanding and well-constraining the vertical distribution of CCN concentration in climate models is crucial for improving modeling of aerosol-cloud interactions (Liu et al. 2012; Penner et al. 2001; Redemann et al. 2021). As seen in Figure 2.4, in situ measurements are not a realistic way to obtain vertically-resolved CCN concentrations. However, lidar has advantages in measuring and retrieving vertically-resolved aerosol properties. If lidar measurements can be used to obtain vertically-resolved

CCN concentrations via forthcoming relationships between in situ CCN concentration and HSRL-2 BSC/EXT, it will greatly aid in testing aerosol-cloud interaction assessments in global climate models.

2.4   Primary Science Questions

To narrow down these big picture goals, this study will address the following science questions (SQs):

1. How are CCN number concentration and HSRL-2 observed aerosol optical properties related in the biomass burning aerosol dominated Southeast Atlantic?;

2. Are relationships between CCN number concentration and aerosol optical properties similar for different parts of the seasonal burning cycle?;

3. Under what conditions do HSRL-2 observed aerosol optical properties provide good constraints for these relationships?;

4. Do relationships between in situ CCN and aerosol optical properties calculated from in situ size distributions agree with relationships between in situ CCN and remotely sensed optics from HSRL-2?

Inherent in these science questions is the hypothesis that 355 nm BSC and EXT from HSRL-2 will have a stronger correlation with CCN concentration due to the shorter wavelength theoretically able to better correspond with small CCN aerosols. SQ (4) will focus on explaining why this hypothesis may or may not be correct.

Chapter 3

Data and Methods

3.1 Data Sets and Instrumentation

This study uses six data sets from a variety of in situ and remote sensing instruments included during the NASA ORACLES campaign. As alluded to in Chapter 2, the three primary variables of interest in this study are CCN concentration and HSRL-2 EXT and BSC. In total there are twenty-two days' worth of data where both data sets are available. Four come from 2016 (20160912, 20160918, 20160920, 20160924), six from 2017 (20170812, 20170813, 20170815, 20170824, 20170826, 20170828), and twelve from 2018 (20180927, 20180930, 20181002, 20181003 20181005, 20181007, 20181010, 20181012, 20181015, 10181019, 20181021, 20181023). A summary of the primary instruments and their corresponding observables is given in Table 3.1.

3.1.1 In Situ Instruments

3.1.1.1 GIT CCN Instrument

The Georgia Institute of Technology (GIT) CCN counter measures CCN concentration at various levels of water vapor supersaturation (Kacarab et al. 2020; Redemann et al. 2021), usually selected by an in-flight instrument operator. This instrument provides in situ measurements of CCN and is designed as a continuous-flow streamwise

Table 3.1: List of instruments and data sets utilized in this study, as well as their respective resolution, measurement type, and aircraft.

Instrument	Variables	Resolution (Temporal/ Vertical)	Measurement Type	Aircraft
High Spectral Resolution Lidar 2 (HSRL-2)	Backscatter Coefficient (355 and 532 nm), Extinction Coefficient (355 and 532 nm)	10 s / 15 m	Remote Sensing	ER-2 (2016), P-3 (2017-2018)
Cloud condensation nuclei (CCN) counter	CCN number concentration at different super-saturations (SS)	1 s	In Situ	P-3
HiGEAR Particle Soot Absorption Photometer (PSAP) and nephelometer	Dry Extinction (450, 550, and 700 nm)	1 s	In Situ	P-3
Edgetech 3-Stage Hygrometer	Ambient Relative Humidity	1 s	In Situ	P-3
HiGEAR Ultra-High Sensitivity Aerosol Spectrometer (UHSAS) and Aerodynamic Particle Sizer (APS)	Aerosol Size Distributions: UHSAS (70-1000 nm); APS (0.8-5μm)	1 s	In Situ	P-3
HiGEAR Aerodyne HR-ToF-aerosol mass spectrometer (AMS)	Mass-to-charge ratio m/z 44 relative to total organics (f44)	1 s	In Situ	P-3

thermal-gradient chamber (CFSTGC; Roberts and Nenes 2005). It was developed to improve upon thermal gradient diffusion cloud chambers while using important features of continuous-flow parallel plate diffusion chambers. Quasi-uniform supersaturation (SS) values at each flow streamline are achieved through differences in thermal and vapor diffusivity, as well as a constant wall temperature gradient. Aerosols that activate into droplets with size greater than 0.5 μm are counted as CCN at the end of the growth chamber.

One distinct feature of this instrument, as described by Roberts and Nenes (2005) is continuous flow that allows for fast sampling (minimum of 1 sample per second). This is especially important for airborne measurements and is an improvement from earlier cloud chambers that could take up to 20 seconds for a single measurement. The instrument also maximizes SS at the centerline of the column, which maximizes droplet growth (Roberts and Nenes 2005). One possible limitation, as noted in a study mapping the operation of this specific CCN counter lies in the optical particle counter (OPC) detection threshold. For slow-growing particles or particles with low critical SS, droplet size may be smaller than what can be detected by the OPC, and this can cause difficulty distinguishing between droplets and interstitial aerosol (Lance et al. 2006).

3.1.1.2   HiGEAR Instrument Suite

Dry extinction, size distribution, and f44 data sets come from the Hawaii Group for Experimental Aerosol Research (HiGEAR) instrument suite. Dry extinction is measured by two Radiance Research particle soot absorption photometers (PSAPs)

and two TSI 3653 nephelometers (Shinozuka et al. 2020; Redemann et al. 2021). The nephelometers measure aerosol light scattering at 450, 550, and 700 nm, and the PSAPs measure light absorption coefficients at 470, 530, and 660 nm. Resultant in situ dry extinction is reported at 450, 550 and 700 nm and then interpolated to match wavelengths given by the HSRL-2 (355 and 532 nm) for more direct comparison.

Two instruments are used to measure in situ aerosol size distributions behind an aerosol inlet, while other optical probes were located under the P-3 wings to measure aerosol size distributions at ambient conditions. The Droplet Measurement Technologies (DMT) ultra-high sensitivity aerosol spectrometer (UHSAS) is an optical-scattering, laser-based spectrometer that measures aerosols with an optical size of 70-1000 nm (DMT 2017). This size range constitutes the fine mode of the size distribution that is most relevant to CCN concentrations (Redemann et al. 2021). The UHSAS laser is used to illuminate particles, and the instrument captures resultant scattering to determine particle size, since amount of light scattered is strongly correlated with particle size (DMT 2017). The TSI 3321 Aerodynamic Particle Sizer (APS) measures aerosols with aerodynamic size of 0.8-5 μm. This range constitutes what we consider to be the coarse mode of the aerosol size distribution (Redemann et al. 2021). Unlike the UHSAS, the APS measures aerodynamic size and relative light-scattering intensity instead of converting light scattering to geometric size, which can cause inaccuracies (TSI 2017). In this study we convert aerodynamic size to geometric size for consistency between data sets.

The mass-to-charge ratio m/z 44 relative to total organics (f44) data set is used to estimate aerosol age and is measured using the Aerodyne high-resolution time-of-flight

(HR-ToF) aerosol mass spectrometer (AMS). This instrument provides quantitative size and chemical mass loading information for non-refractory sub-micron aerosol particles. One advantage to this instrument is the ability to combine information about particle aerodynamic diameter and composition in a single measurement due to mass spectrometer detection that is combined with particle time-of-flight information (Aerodyne 2021). The f44 data set is available for all days of overlap between CCN and HSRL-2 except for 20170812 and 20170828, where there is no salvageable AMS data.

3.1.2 Remote Sensing Instruments

3.1.2.1 HSRL-2

The NASA Langley Research Center multi-wavelength HSRL-2 is a remote sensing instrument deployed on the ER-2 during 2016 and the P-3 during 2017 and 2018. From its measurements we will utilize particulate BSC and EXT at 355 and 532 nm and lidar ratio, an extinction to backscatter ratio available at both wavelengths (Redemann et al. 2021). The HSRL-2 measurement technique is updated and improved in comparison to standard backscatter lidars through use of the spectral distribution of the return signal to distinguish between aerosol and molecular returns. This means that aerosol BSC and EXT coefficients are determined independently as opposed to being a result of a lidar ratio assumption (Hair et al. 2008). The HSRL-2 is a successor to the first NASA Langley airborne HSRL-1 with updated capability to use the HSRL technique described by Hair et al. (2008) at 355 nm in addition to the original

532 nm wavelength in HSRL-1. This wavelength is more sensitive to smaller particles, such as CCN, that are especially relevant in aerosol-cloud interactions (Burton et al. 2018). Horizontal resolution of HSRL-2 products is approximately 2 km, and reported vertical resolution is 15 m.

3.2 Data Collocation

This study will focus on analyzing relationships between CCN number concentration and HSRL-2 BSC and EXT coefficients. HSRL-2 profiles were observed from high-altitude, above-plume flight legs, while CCN concentration was measured in situ at lower altitudes, in and around the smoke plume. Therefore, before beginning correlative analysis we must develop a method to collocate both data sets in time and space. One data collocation consideration is the difference in aircraft flown between 2016 and 2017-2018. In 2016 the HSRL-2 was located on the ER-2 and in situ instruments on the P-3. However, in 2017-2018 both instruments were located on the P-3. Since the P-3 flew at above-plume altitudes while the HSRL-2 was measuring and later returned to lower altitudes for in situ measurements, there is a slightly larger time gap between data availability during those years.

The end goal of data collocation is to have one average CCN concentration value to directly compare with one average HSRL-2 observation, both observed in approximately the same time and space that we define using three independent collocation criteria. For any given HSRL-2 profile, the collocation method finds CCN measurements that fall within a set amount of time (dt) from when the HSRL-2 profile was

measured, within a set horizontal distance (dd) from the profile, and within set vertical bins (dh). CCN concentration and HSRL-2 BSC and EXT values that remain after each of these criteria have been applied are then averaged to allow for a one-to-one comparison. A schematic of this process is shown in Figure 3.1. Note that while each year uses the same collocation method, 2017 and 2018 have a different aircraft set-up that results in a longer time gap between measurements (denoted by t + Δt).
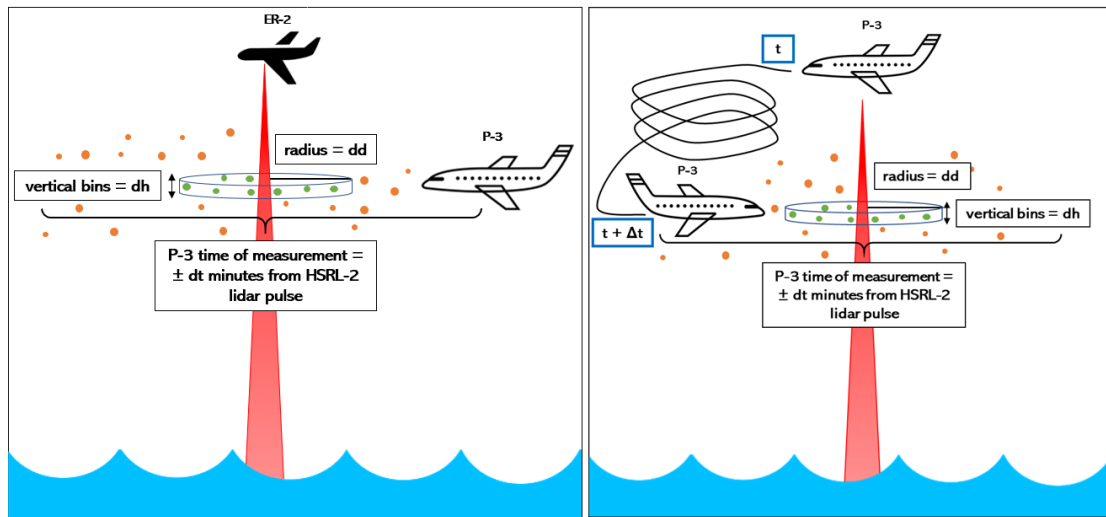
Figure 3.1: Graphic depicting data collocation process for a) 2016 and b) 2017 and 2018. CCN that fall within the time, horizontal distance, and vertical bin criteria (green points) are averaged to compare to the average HSRL-2 BSC and EXT coefficients in each HSRL-2 pulse that fall within the same vertical bin.

In Chapter 4 we will present sensitivity testing analyses to explore the implications of using different collocation criteria values and the steps taken to maximize correlation in resultant linear relationships between CCN concentration and HSRL-2 coefficients. The final values, post sensitivity testing, are given in Table 3.2 and will be used for all ensuing results. We have chosen to hold horizontal distance constant at ±1.1 km for all years to approximately correspond with the horizontal distance

over which HSRL-2 product is aggregated, as well as to not average HSRL-2 profiles in the horizontal. Therefore, each average CCN concentration value corresponds to a vertical average of BSC and EXT coefficients from one profile. Vertical bin size varies slightly due to adjustments made to optimize correlation, and time values are increased for 2017 and 2018 largely due to the longer time gap between data availability.

One final step taken before looking at results is to eliminate data points that do not have all four HSRL-2 coefficients of interest (EXT and BSC at 355 and 532 nm) available. This ensures a fair comparison using the same amount of data for both coefficients at both wavelengths.

3.3   Data Filtering

Additional aspects of this analysis that will be detailed further in Chapter 4 are considerations about ambient relative humidity (RH) and CCN counter SS levels. In general, results suggest that high RH values tend to weaken the CCN vs. HSRL-2 relationship due to highly hygroscopic aerosols. As hygroscopic aerosols swell in humid conditions, BSC and EXT tend to increase without a corresponding increase in CCN concentration. This will be demonstrated in Section 4.1.1. Consequent RH sensitivity testing leads to our focus on measurements made in relatively dry conditions, RH$\leq$40% for 2016 and 2017 and RH$\leq$50% for 2018 (Table 3.2).

Varying SS values used by the CCN counter can also impact the CCN vs. HSRL-2 relationship. In general, Köhler theory suggests that higher SS allows for more

aerosols to activate into droplets. As shown in Section 4.1.2, lower SS values that do not allow for as many aerosols to activate can correspond to increased aerosol concentration and, thus, increased BSC and EXT. This, again, can weaken the CCN vs. HSRL-2 relationship. Addressing this issue is complicated by different SS values and ranges used during each year of the campaign. However, in general we find that measurements made between about 0.2-0.4% SS result in strongest correlation. Sensitivity testing of various SS levels will be explored in Chapter 4, and resultant final values chosen for each year are shown in Table 3.2.

While one goal of the data filtering step is consistency between each year of the campaign, a few differences in data collection and availability make it necessary to slightly alter the RH and SS thresholds between each year. For example, RH filtering varies due to amount of data collected at different RH ranges. While 2016 data spans nearly the entire RH range, 2017 and 2018 have fewer data points collected at very high RH. As for differences in SS filtering, this is largely due to consistent point values being tested by the CCN counter in 2016, while 2017 and 2018 tested a wider range of SS values.

3.4   Mie Theory Calculations

To address the fourth science question involving backscatter and extinction calculated from Mie theory, two different approaches will be taken. Both assume a bimodal size distribution, with each mode used to calculate median radius (r_m) and geometric

Table 3.2: Final collocation criteria, relative humidity, and supersaturation thresholds chosen to analyze each year of ORACLES. Percentage of the entire data set represented by each relative humidity threshold, percentage of the collocated data set represented by each supersaturation threshold, as well as final dates and quantity of data points also given.

	2016	**2017**	**2018**
horizontal criteria (dd)	± 0.01°	± 0.01°	± 0.01°
vertical bin size (dh)	45 m	60 m	75 m
time criteria (dt)	± 0.1 hr	± 0.3 hr	± 0.2 hr
relative humidity (RH)	RH ≤ 40%	RH ≤ 40%	RH ≤ 50%
supersaturation (SS)	SS = 0.30%	0.22% ≤ SS ≤ 0.34%	0.23% ≤ SS ≤ 0.40%
% of data measured below RH threshold (all)	78%	72%	43%
% of data measured below RH threshold (with CCN available)	75%	60%	49%
% of collocated data set in SS range	76%	72%	66%
# of days represented in collocated data set (after RH and SS filtering)	1 (20160912)	3 (20170812, 20170815, 20170828)	6 (20180927, 20181002, 20181007, 20181010, 20181019, 20181023)
# of data points (after RH and SS filtering)	40	14	27

standard deviation (σ_g). These parameters, in addition to aerosol-type specific refractive indices, are input to Eqns. 1.2 and 1.3 to calculate backscatter and extinction coefficients from Mie theory.

A schematic showing the primary steps for each method is shown in Figure 3.2. The first approach starts with in situ size distribution measurements from the UHSAS and APS. The UHSAS measures fine mode aerosols ($70\ nm - 1000nm$) and the APS measures coarse mode aerosols ($0.8\ \mu m$ - $5\ \mu m$). Defining fine and coarse modes with these size ranges will cause our theoretically calculated backscatter and extinction to be smaller in magnitude than what is observed by HSRL-2 since those measurements account for all atmospheric aerosols unconstrained by size bins. However, using these size ranges in calculations will still represent how each mode contributes to total optics. Next, r_m and σ_g can either be calculated from effective radius (r_{eff}) and variance (v_{eff}), or by fitting a lognormal distribution to each observed size distribution. Due to the noisiness of many in situ size distribution measurements, we found in this case that calculating r_m and σ_g directly from r_{eff} and v_{eff} for each size mode is the more reliable method. Equations (3.1) to (3.5) below show the necessary steps for these calculations.

$$r_{eff} = \frac{\int_{r_1}^{r_2} r^3 n(r)\, dr}{\int_{r_1}^{r_2} r^2 n(r)\, dr} \tag{3.1}$$

$$v_{eff} = \frac{\int_{r_1}^{r_2} (r - r_{eff})^2 r^2 n(r)\, dr}{r_{eff} \int_{r_1}^{r_2} r^2 n(r)\, dr} \tag{3.2}$$

$$\sigma_g = \sqrt{ln(v_{eff}+1} = ln(S) \tag{3.3}$$
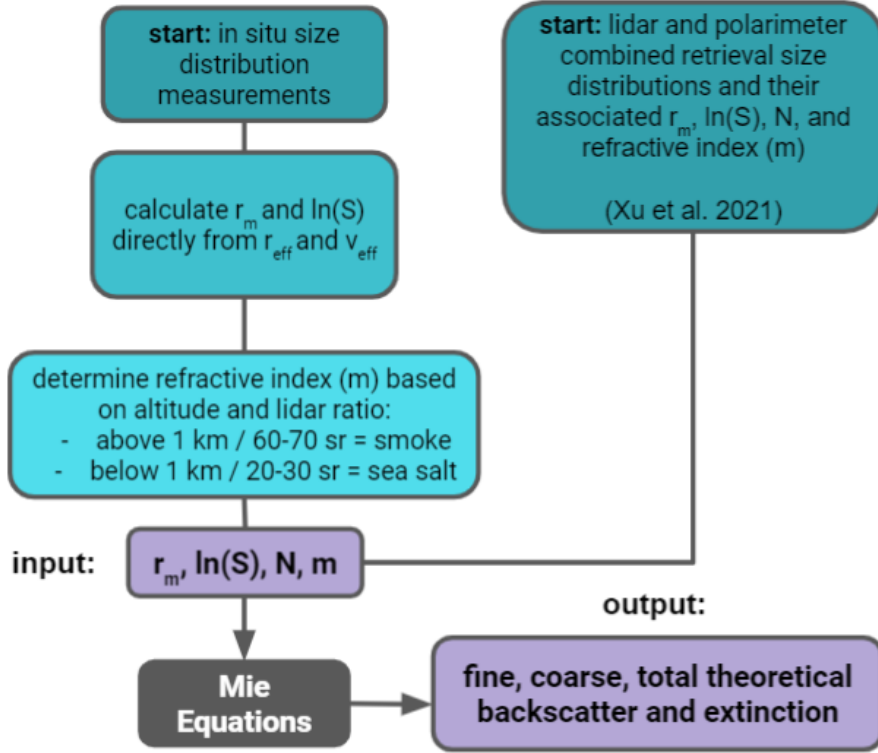
Figure 3.2: Flowchart displaying steps taken to calculate theoretical backscatter and extinction coefficients given two starting points – in situ size distributions or lidar and polarimeter combined retrieval size distributions.

$$r_g = \frac{r_{eff}}{exp(5\sigma_g^2/2)} \tag{3.4}$$

$$r_m = exp[ln(r_g) + 3\sigma_g^2/2] \tag{3.5}$$

The starting point is Eqn. 3.1, where r is any given bin center radius, and $n(r)dr$ is particle number concentration within each size bin. From effective radius, an effective variance can be calculated (Eqn. 3.2). In turn, we use each of these values to calculate a geometric variance (represented by either σ_g or $ln(S)$) and radius (Equations (3.3)

and (3.4)). These values are then used to calculate median radius, as shown in Eqn. 3.5.

The alternate starting point is retrieved size distributions and their associated r_m and σ_g from combined lidar and polarimeter retrievals by Xu et al. (2021). Their retrieval algorithm updates and adjusts size distributions dynamically. Since retrieval optimization aims to fit all lidar signals simultaneously with the best set of aerosol properties, retrieved aerosol intrinsic properties can well reproduce lidar signals. This method also tends to better represent coarse mode than the in situ measurements. Retrievals from this study are available for ORACLES 2016 in cases determined to be cloud-free. We will use retrieval data available for 2016 and compare to results obtained using in situ size distributions. For 2017 and 2018 we will solely use the in situ size distribution method.

After r_m and σ_g are calculated using one of these methods, the final parameters needed are aerosol-specific refractive indices. For both methods we assume a wavelength invariant refractive index determined by the combined lidar and polarimeter retrievals (Xu et al. 2021). These are shown in Table 3.3. When using in situ size distributions we utilize these values based on altitude and lidar ratio of the measured size distribution. Typically, the marine boundary layer and associated sea salt aerosols exist between the surface and 1 km, while smoke aerosols are found above 1 km. Since this does not always perfectly hold, we also refer to lidar ratios when picking an altitude cut off for refractive indices. We expect lidar ratio for pure smoke aerosols to be 60+ sr, while sea salt has a lidar ratio between 20-30 sr (Omar et al.

Table 3.3: Real and imaginary components of combined lidar polarimeter retrieved refractive indices for biomass burning aerosols and sea salt. Values from combined lidar-polarimeter retrievals (Xu et al. 2021).

	Biomass Burning Aerosol (fine mode)	Biomass Burning Aerosol (coarse mode)	Sea Salt (fine mode)	Sea Salt (coarse mode)
real	1.58	1.37	1.415	1.363
imaginary	0.03	0.00001	0.002	0.00001

2009). For each years' collocated data set, lidar ratio values suggested that we are primarily looking at smoke aerosols.

Once r_m, σ_g and a refractive index are determined for each collocated data point (or each available data point if using retrieved size distributions), these parameters, plus total number concentration, are the input to Mie scattering equations. As output we look at total backscatter and extinction coefficients at 355 and 532 nm, as well as those coefficients separated into contributions from fine and coarse modes.

Chapter 4

Results

4.1 Data Processing Choices

The method with which CCN and HSRL-2 datasets are collocated was outlined in Section 3.2. Conditions under which HSRL-2 observations provide good constraints for inferring CCN concentration will be identified by looking for RH limits, SS thresholds, and combinations of collocation criteria that optimize the CCN vs. HSRL-2 relationship. The values determined as being "optimal" were discussed in Chapter 3, shown in Table 3.2, and will be used for most of this analysis. However, the goal of this section is to take a step back and explain the methodology and justification behind the final chosen values.

The subsequent steps and decisions summarize numerous stages of trial and error with various combinations of RH limits, SS thresholds, and collocation criteria values and will be organized as follows: Section 4.1.1 will discuss RH dependence and Section 4.1.2 will investigate the implications of CCN counter SS values. Section 4.1.3 will test a range of collocation criteria values to determine a final set of criteria that are optimal and reasonable for each year of the campaign. Since ambient RH and instrument SS are related to inherent physical limitations of remote sensing and aerosol nucleation, we explore those data filtering steps first at a set of baseline collocation criteria given

in Table 4.1. These values serve as a reasonable place to start and will be narrowed down further in Section 4.1.3.

Sections 4.1.1-4.1.3 show results for EXT at 355 nm and will continue to use this coefficient as an example of results for each stage of sensitivity testing. This is done to keep sensitivity testing results as straightforward as possible. Furthermore, the forthcoming patterns and trends are nearly identical across all four coefficients, unless otherwise noted. All wavelengths and coefficients will be compared more thoroughly after sensitivity testing decisions are made.

Table 4.1: Baseline criteria used to explore sensitivity testing of different data filtering steps for each year. These values were chosen and hypothesized to be reasonable for each year based on initial testing.

	dt	dd	dh
2016	± 0.1 hr	± 0.01°	45 m
2017	± 0.3 hr	± 0.01°	45 m
2018	± 0.2 hr	± 0.01°	45 m

4.1.1   Relative Humidity Dependence

The top row of Figure 4.1 shows initial results after collocating datasets but before making any further data filtering decisions for 2016, 2017, and 2018. The data points are color coded by RH and there are a couple of key features noticeable at first glance. First, for each year and set of baseline criteria, we see the semblance of a linear relationship between the two variables. This supports the idea that our data collocation technique and initial choice of collocation criteria are reasonable. Second, we notice a pattern that seems to be weakening the CCN vs. EXT at 355 nm relationship. While most apparent in 2016, where we have the most data points

35

available (Figure 4.1a), each year shows a grouping of points measured at high ambient RH that correspond to increased EXT and low CCN concentrations. As mentioned in Section 3.3, this feature is likely due to hygroscopic aerosols that absorb water and swell to cause an increase in BSC and EXT while not increasing CCN concentration. Since a primary goal is optimization of this CCN vs. HSRL-2 relationship, ambient RH will be filtered to avoid this occurrence that causes the linear relationship to break down.

The bottom row of Figure 4.1 shows a similar analysis, but for restricted SS ranges. To avoid conflating effects of RH and SS, these restricted SS ranges (0.2-0.3% for 2016 and 0.3-0.4% for 2017 and 2018) are not equivalent to how we will ultimately filter SS but are chosen to demonstrate that when varying SS is not a factor, the hygroscopicity impacts of RH are still evident. This result is most obvious for 2016 and might have been clearer for 2017 and 2018 if more collocated data points were available.

Figure 4.2 shows a series of RH filtering trials for 2016. We start by removing data points with RH$\geq$60% based on using Figure 4.1 to make a first estimate of what a sufficient threshold might be (Figure 4.2a). We then narrow down the dataset further to filter out RH$\geq$40% (Figure 4.2b). For this set of baseline collocation criteria, no collocated data points have an average ambient RH between 50-60%, so we skip that multiple of 10%. We also do not filter out RH at values lower than 40% to avoid eliminating too much of the dataset. If only evaluating Figure 4.2, results show that using data with RH$\leq$60% produces strongest correlation. However, this is one of many instances in which previous rounds of trial and error have shown that SS

36
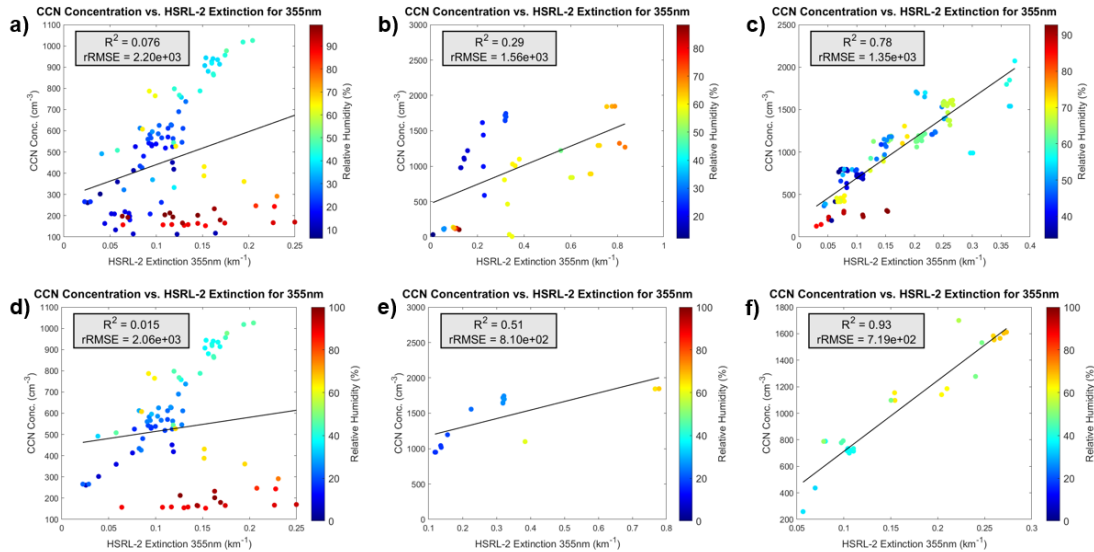
Figure 4.1: CCN concentration vs. HSRL-2 EXT at 355 nm for a/d) 2016, b/e) 2017, and c/f) 2018. In the top row (a-c), results are not filtered by RH or SS. High RH points with high EXT and low CCN concentration signify highly hygroscopic aerosols that tend to weaken the relationship (top row). In the bottom row (d-f), results are not filtered by RH, but SS is constrained to 0.2-0.3% for 2016 and 0.3-0.4% for 2017 and 2018. This row is shown to avoid conflating effects of RH and SS. Here we see that at even at a restricted SS range, the effects of high RH on hygroscopicity are still evident, though sometimes to a lesser extent. Note that figure axes are not equivalent between years.

filtering will give nearly identical results for 2016 regardless of which RH threshold is chosen, and that an RH bound of 40% is ideal for 2017 results. When considering this secondary goal of pursuing continuity where possible when filtering three years of data, this will be the final factor used to determine that 2016 analysis will only consider data points measured at an ambient RH≤40%.

The approach taken for 2017 is very similar. Figure 4.3 shows a first approach at eliminating the high RH effect by narrowing down our RH range to be less than or equal to 60%, 50%, and 40%. Unlike 2016, the trend is clearer in this case that
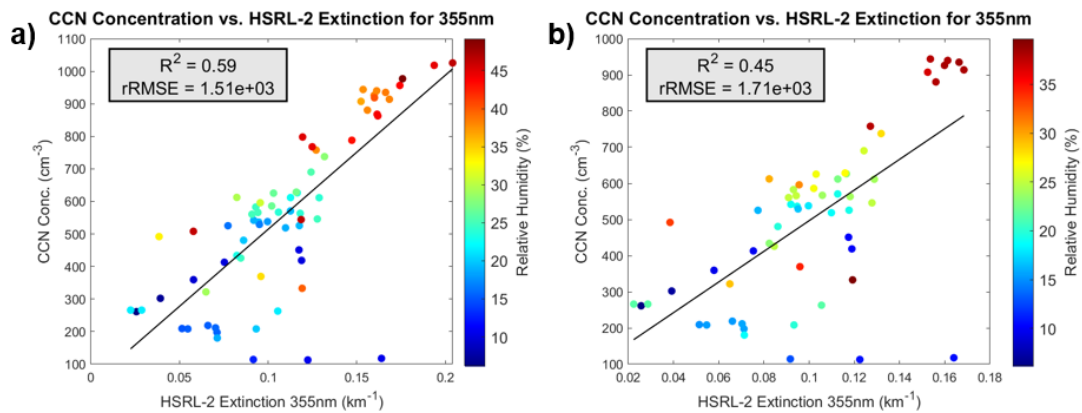
Figure 4.2: 2016 CCN concentration vs. HSRL-2 EXT at 355 nm for a) RH≤60% and b) RH≤40%. This collocated dataset has no relative humidity values between 50-60%. Note that figure axes are not equivalent between different filtering steps.

as maximum RH values in the dataset decrease, correlation increases. For 2017, narrowing down the dataset to only include measurements made at RH≤40% is optimal and this is the value that will be used moving forward.
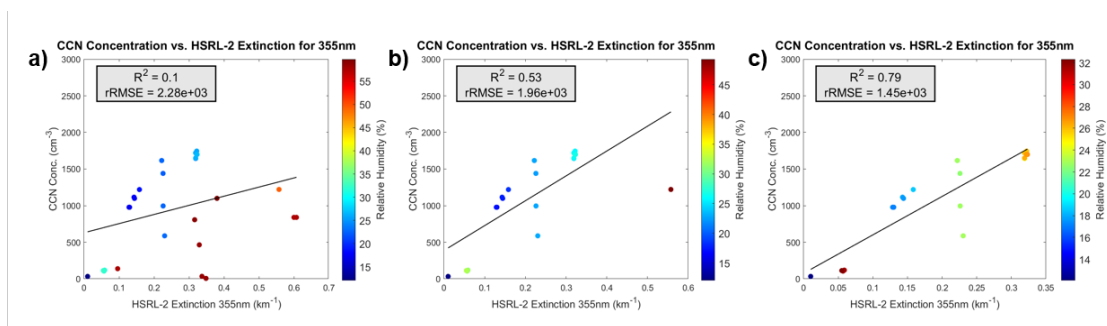
Figure 4.3: 2017 CCN concentration vs. HSRL-2 EXT at 355 nm for a) RH≤60%, b) RH≤50%, and c) RH≤40%. Note that figure axes are not equivalent between different filtering steps.

As for 2018, Figure 4.1 shows that the effects of hygroscopic aerosols are present but not quite as prevalent as they are for the previous two years. Nevertheless, to address the few high RH data points Figure 4.4 shows results for data with RH less

than or equal to 60%, 50%, and 40%. Unlike the other years, the strongest correlation in this case occurs when looking at the dataset captured by RH≤50% (Figure 4.4b). Due to two primary clusters of data, less overall spread, and a very small resultant RH range, using RH≤40% results in a very weak relationship. Therefore, 2018 analysis will filter out data measured at an ambient RH above 50%.
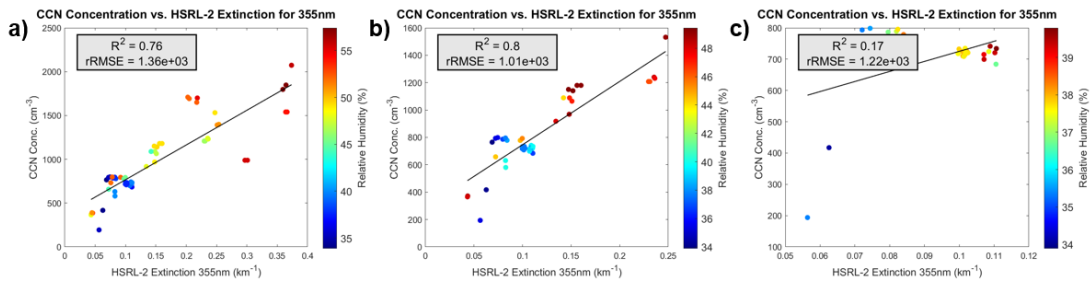
Figure 4.4: 2018 CCN concentration vs. HSRL-2 EXT at 355 nm for a) RH≤60%, b) RH≤50%, and c) RH≤40%. Note that figure axes are not equivalent between different filtering steps.

The decision to only analyze data measured at relatively low RH values is not one made without regard to the resulting representativeness of the remaining dataset. Table 3.2 shows the amount of total data for each year that was measured at each respective RH threshold. For 2016 and 2017, these thresholds still allow us to consider more than half of the dataset. For 2018, data measured at an RH≤50% constitutes slightly less than half of the entire dataset available for that year. One possible limitation inherent in this data filtering step is that our resultant CCN vs. HSRL-2 relationships will not be accurate for CCN measured at high ambient RH. This likely means that we are not considering or understanding how CCN concentrations near the cloud base are related to HSRL-2 BSC and EXT. Aerosols located in this humid, near

cloud base region are especially important to cloud droplet formation but are subject to complex processes such as the humidification effect and cloud processing and are therefore excluded from this study. This is one drawback of our chosen technique and would be interesting for future analysis.

4.1.2 Supersaturation Dependence

Another aspect of the data processing step involves the SS values tested by the CCN counter. In 2016, the CCN counter was operated at three discrete SS values, 0.1%, 0.2%, and 0.3%, but 2017 and 2018 use varying ranges of SS values that are not identical between different days. As we investigate the impacts that different SS values have on the relationship between CCN concentration and HSRL-2 BSC and EXT, we will use a similar approach for each year while also recognizing the inherent differences due to CCN counter operation discrepancies.

Figure 4.5 shows the 2016 relationship between CCN concentration and EXT at 355 nm for baseline collocation criteria, with the dataset already filtered to remove RH≤40%. One of the most noticeable results here is that data points measured at the highest SS (0.3%) tend to fall closest to the line of best fit and appear to have less spread, while the lowest SS (0.1%) characterizes data that most clearly is weakening the relationship. The low SS points also correspond to high EXT coefficients, which can be understood by recognizing that the lidar measures all particles in any given atmospheric column. For a given size distribution and aerosol composition, SS determines the critical diameter of activation. At a low SS, critical diameter is larger and resultant CCN concentration is lower. Looking at the R^2 for each individual SS value

40

shows that the two lowest values result in the lowest R^2 when compared to that for 0.3%. Therefore, to optimize these relationships, the 2016 analysis will only include CCN measured at this highest SS value.
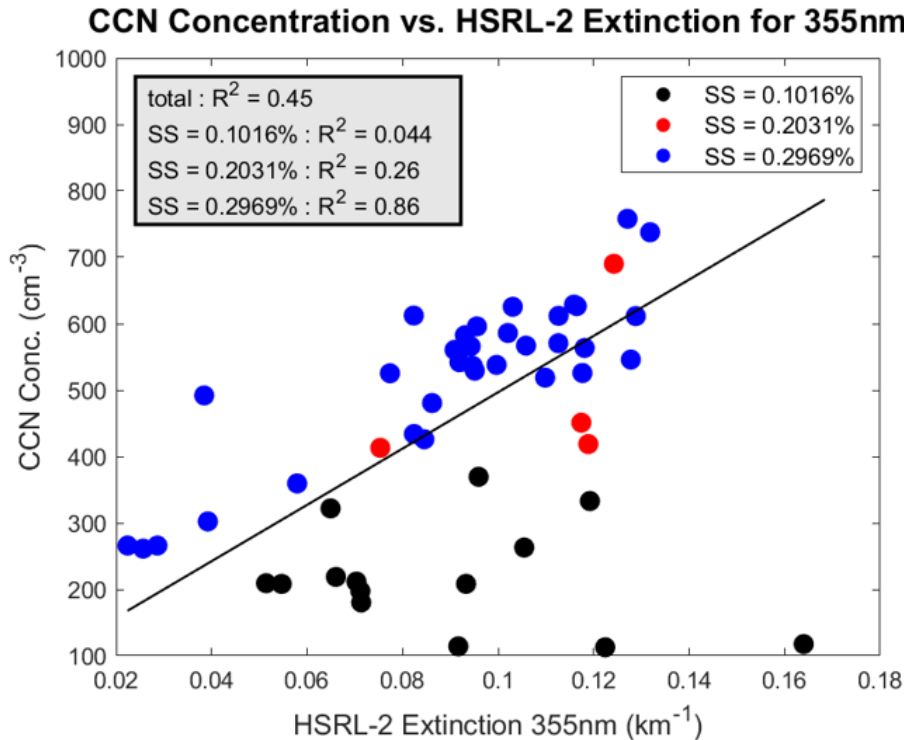
Figure 4.5: 2016 CCN concentration vs. HSRL-2 EXT at 355 nm for RH≤40%. Three discrete supersaturation values are color-coded. Lowest supersaturation value (0.1016%) appears to be weakening the relationship, as opposed to the highest supersaturation value (0.2969%) that allows more aerosols to nucleate into CCN.

Since 2017 and 2018 use a range of SS values instead of three discrete values, Figures 4.6 and 4.7 show results for 2017 and 2018, respectively, with ranges of SS shown by different colors. Again, these relationships are given for the same baseline collocation criteria, with the datasets filtered to remove RH values above 40% (2017) and 50% (2018). These results do not offer the same clear-cut distinction between supersaturation values that was apparent in 2016. Low SS outliers do not as clearly

weaken the relationship. Therefore, the approach to narrowing down which SS values to consider will be motivated by two goals: 1) we are still interested in optimizing the CCN concentration and HSRL-2 relationship, due to the end goal of using HSRL-2 BSC and EXT coefficients to accurately estimate CCN concentrations, and 2) we want to keep the approach taken between all years as consistent as possible.
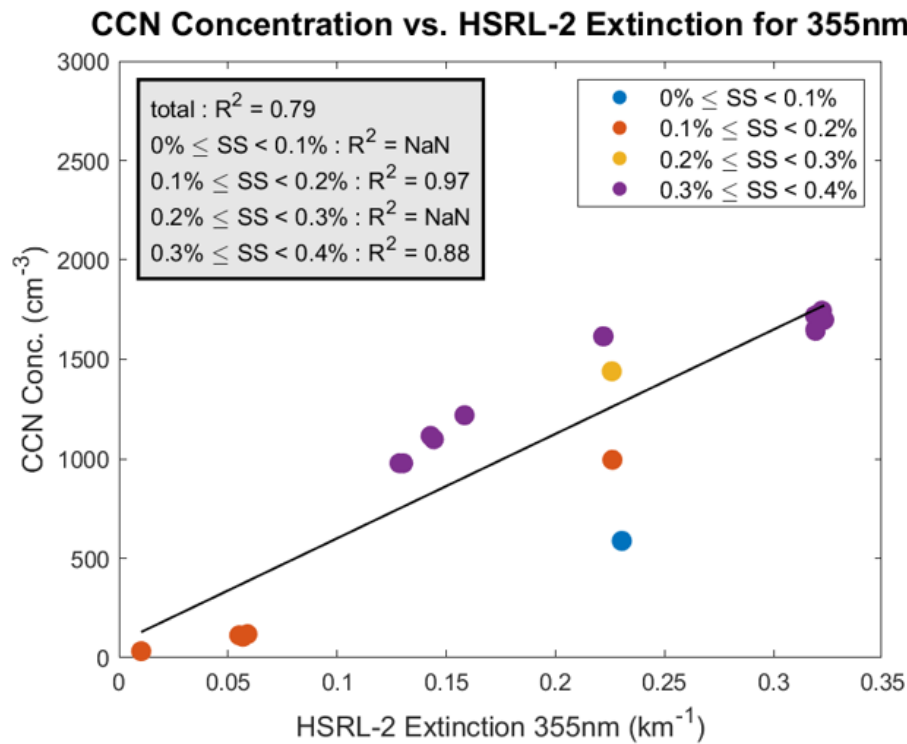
Figure 4.6: 2017 CCN concentration vs. HSRL-2 EXT at 355 nm for RH$\leq$40%. Four supersaturation ranges are color-coded. Although not as distinct as in 2016, lower supersaturation values tend to weaken this relationship.

With these goals in mind, looking at Figure 4.6 shows that data in the 0-0.1% and 0.1-0.2% ranges fall furthest from the line of best fit. Again, we know that low SS values allow for fewer aerosols to activate as CCN. Like 2016, we want to keep the higher values in the analysis and see that data points in 0.2-0.3% and 0.3-0.4% ranges
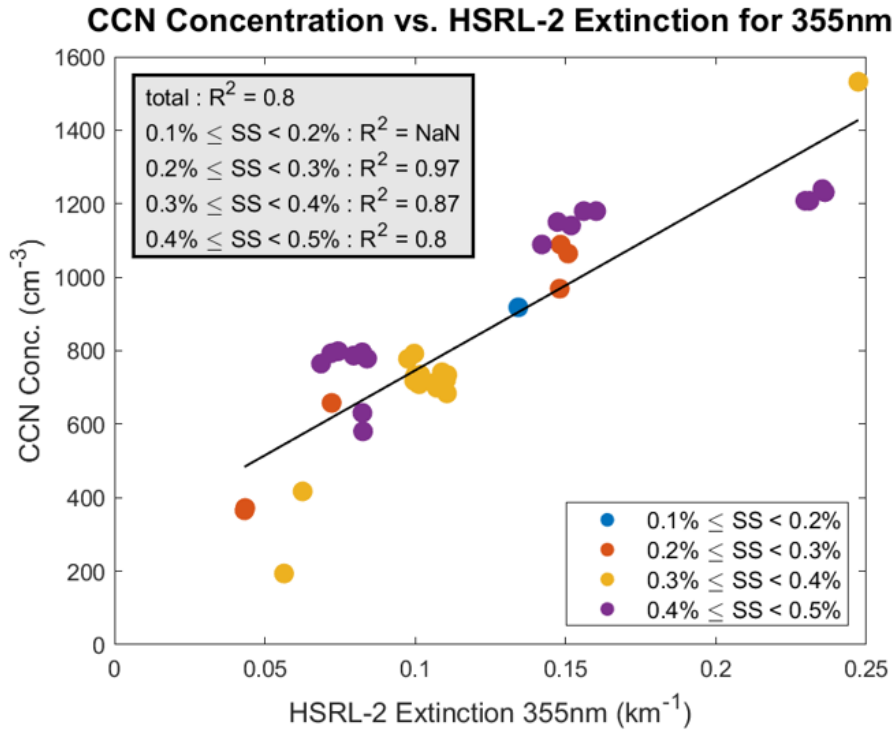
Figure 4.7: 2018 CCN concentration vs. HSRL-2 EXT at 355 nm for RH≤50%. Four supersaturation ranges are color-coded. High supersaturation values above 0.4% tend to weaken this relationship.

all fall close to the line of best fit with relatively high R^2 values. Therefore, the 2017 analysis will only consider SS≥0.2%. Therefore, the 2017 analysis will only consider SS≥0.2%, and after final collocation criteria are applied this threshold results in a range of SS between 0.22-0.34% (Table 3.2).

Like 2017, the SS filtering process for 2018 is less straightforward. Figure 4.7 shows color-coded SS ranges for 2018 baseline collocation criteria and for data measured at RH≤50%. Minor discrepancies exist between BSC and EXT results for each SS range, but overall omitting SS≥0.4% results in stronger relationships across all four coefficients. Furthermore, it was seen in preliminary tests using different combinations of collocation criteria that SS values above 0.4% tend to act as outliers that weaken

the linear relationship, perhaps because 2018 has the widest range of SS values tested that can reach up to 1%. Therefore, although another slightly subjective decision, we believe it to make sense to remove the highest SS values that do not overlap with 2016 and 2017 values from 2018 analysis. After final collocation criteria are applied, this SS threshold results in a range of SS between 0.23-0.40% (Table 3.2).

As with RH filtering, it is important to recognize that only using a subset of SS values impacts the representativeness of the dataset. Table 3.2 shows the percent of each collocated dataset that remains once filtering SS to the values and ranges explored in this section. These percentages are given for our final collocation criteria that are similar, but not identical, to the baseline criteria used in this section. Nevertheless, the SS values that remain in the analysis represent more than half of the collocated dataset across all years of the campaign.

4.1.3 Collocation Criteria Sensitivity Testing

As mentioned in Chapter 3, no year of the ORACLES campaign has perfectly synchronous HSRL-2 and CCN data. Though both measurements were made in approximately the same time and location, they still need to be collocated before analyzing relationships between both variables. Section 3.2 discusses this method in detail and outlines the final criteria chosen for the analysis. This section will explore the implications of changing these criteria and explain the motivation behind the final sets of criteria chosen for each year. While changing any given criterion, the remaining two will be held constant at the baseline collocation criteria (Table 4.1).

4.1.3.1 Time Range

The time range criterion refers to the amount of time elapsed between when any given HSRL-2 profile is observed and when CCN concentrations are measured. For example, a time value of ± 6 minutes means that CCN concentrations values taken from 6 minutes before to 6 minutes after the HSRL-2 profile are considered in the averaging. The idea in approaching this part of the technique is to keep the time range as short as possible to minimize hypothesized CCN inhomogeneity. In the forthcoming sensitivity testing, we start with a time criterion of ± 6 minutes for 2016 and 2018 and ± 18 minutes for 2017, increasing the range in increments of ± 6 minutes (or ± 0.1 hour). ± 6 and ± 12 minutes are not shown for 2017 because no data points are available at those values.

Results for these analyses are shown in Figure 4.8. The primary pattern for all years is that as time between HSRL-2 and CCN measurements increases, the strength of the relationship decreases, often rapidly. This supports the hypothesis of significant temporal heterogeneity of CCN, as the shortest time periods tested continuously result in the strongest correlation. Consequently, the time criterion that will be selected for future analysis are ± 6 minutes for 2016, ± 18 minutes for 2017, and ± 12 minutes for 2018. These values match the baseline criteria used previously, as preliminary testing suggested that these were the shortest time periods possible to use for each year.

Figure 4.8: CCN concentration vs. HSRL-2 EXT at 355 nm at various time criteria values for a) 2016, b) 2017, and c) 2018. For each year, strength of the relationship decreases as amount of time considered increases. Note that figure axes are not equivalent between years.

4.1.3.2 Horizontal Distance

The horizontal distance criterion refers to the horizontal, radial distance around any given HSRL-2 profile within which remaining CCN measurements fall after time collocation. For example, a value of ±1.1 km means that CCN concentration values within ±1.1 km in any horizontal direction of an HSRL-2 profile are considered in the corresponding average. The baseline horizontal distance value is ±1.1 km ($\pm0.01°$, as this is roughly equal to the horizontal distance over which the HSRL-2 product is data aggregated. From here we will investigate results for increasing increments of $\pm0.03°(\pm3.3$ km).

Results for these analyses are shown in Figure 4.9. 2016 results show that as horizontal distance increases, the strength of the CCN vs. HSRL-2 relationship stays relatively constant. There is a slight increase between ±1.1 km and ±4.4 km, followed by slight fluctuation in R^2, but no drastic changes. 2017 and 2018 show slightly different results. For 2017 there is a steady and higher magnitude decrease in R^2

values as horizontal distance increases, while 2018 shows a large drop between ± 1.1 km and ± 4.4 km with slightly higher but fluctuating results at longer distances.

Despite these horizontal distance discrepancies, results support the choice of ± 1.1 km in all years as the horizontal distance that will result in the strongest relationships. Weakening of the CCN vs. HSRL-2 relationship may suggest increased CCN heterogeneity at longer distances or could be due to the collocation methodology. Since our method averages HSRL-2 BSC and EXT in the vertical, but not in the horizontal, results shown using longer horizontal distances compare CCN concentration in a large area to a singular HSRL-2 profile. When only considering a horizontal distance of ± 1.1 km from any given HSRL-2 profile, this approximately corresponds to the horizontal distance over which HSRL-2 data is aggregated for one profile, assuring more of a one-to-one comparison between average CCN concentration with average BSC and EXT from one profile.
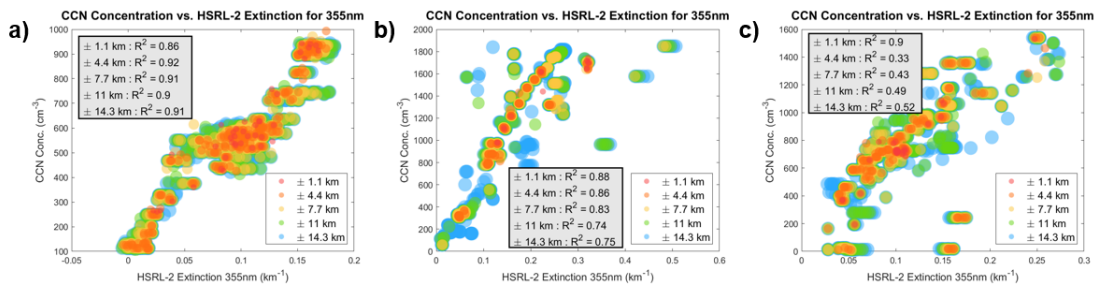
Figure 4.9: CCN concentration vs. HSRL-2 EXT at 355 nm at various horizontal distance criteria values for a) 2016, b) 2017, and c) 2018. Results in 2016 stay relatively constant as horizontal distance increases, while in 2017 and 2018 increased horizontal distance tends to weaken the correlation. Note that figure axes are not equivalent between years.

4.1.3.3 Vertical Bin Size

The vertical bin size criterion refers to the vertical depth over which CCN concentration and HSRL-2 values that also meet the time and horizontal distance criteria are averaged. Since the vertical resolution of HSRL-2 BSC and EXT is 15 m, our baseline vertical bin size is 45 m to make sure that vertical spacing is not too close to altitude measurement uncertainty. From here we will test values in increasing increments of 15 m.

Results for these analyses are shown in Figure 4.10. The strength of the CCN vs. HSRL-2 relationship does not appear to be significantly dependent on changes in vertical bin sizing for any year. Although minor fluctuations do occur, no specific bin size results in considerable heterogeneities that weaken the overall relationship. Therefore, selection of vertical collocation criteria is solely dependent on which value appears to result in slightly stronger correlations overall. This leads to the selection of 45 m for 2016, 60 m for 2017, and 75 m for 2018.
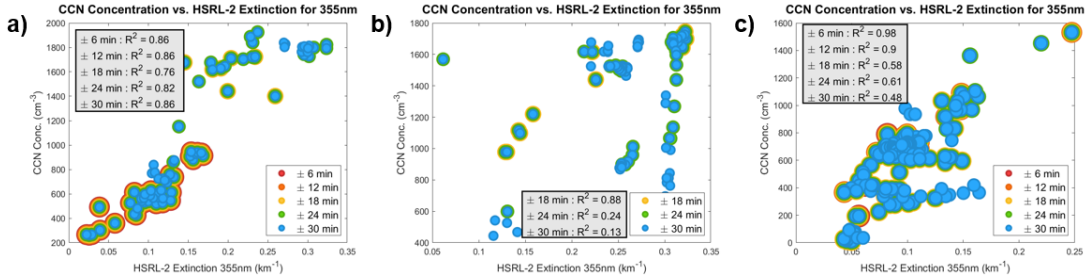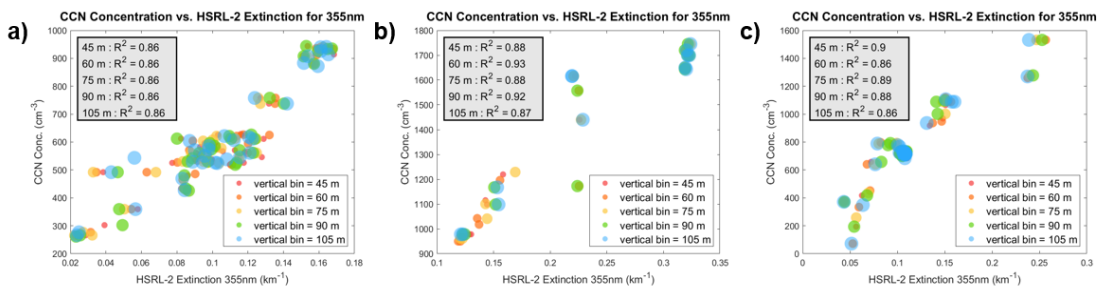

Figure 4.10: CCN concentration vs. HSRL-2 EXT at 355 nm at various vertical bin sizes for a) 2016, b) 2017, and c) 2018. Results for each year show that there are not drastic differences in correlation for different bin sizes. Note that figure axes are not equivalent between years.

4.2 CCN vs. HSRL-2 Extinction and Backscatter

Until this point, results have primarily focused on how the relationship between CCN concentration and HSRL-2 EXT (and BSC) changes under various RH and SS thresholds, as well as the implications that increased time, horizontal distance, and vertical bin size values have on collocation. These steps have narrowed down our data set and demonstrated the conditions under which HSRL-2 observations provide constraints to the relationship with CCN over the BBA dominated SEA. The final values used to filter and collocate data for each separate campaign year are given in Table 3.2. From this section forward, these values will be fixed, and the focus will shift to a comparison of CCN vs. HSRL-2 relationships between different years and at different wavelengths. The implications for our ability to form these relationships will be further explored in Chapter 5.

Using the finalized data filtering values given in Table 3.2, results for 2016, 2017, and 2018 are shown in Figures 4.11 to 4.13, respectively. These figures show the resultant relationships between CCN concentration and HSRL-2 EXT and BSC, with both 355 and 532 nm compared on the same panel. Overall, it is encouraging to see similar relationships emerge between these variables for each year of the campaign after having taken time to investigate differences in data collocation, RH, and SS. In general, as CCN concentration increases, EXT and BSC do as well. Another common pattern, though it does not always hold perfectly, is low RH values associated with low CCN and low BSC and EXT values, while higher CCN concentration and BSC and EXT values are commonly associated with high RH.

Interestingly, 2017 has the strongest relationships overall despite the differences in data collection that were initially hypothesized to weaken the correlation (Figure 4.12). This may in part be due to the small number of data points available (13), but confidence in these results can be found in having three days represented by the relatively small number of data points. Results for 2016 give similar correlation coefficients, although slightly lower than 2017 (Figure 4.11). The resultant 2016 dataset is made up of 40 data points that represent one day. As described in Sections 4.1.1, 4.1.2, and 4.1.3, we have supported reasoning for the data filtering and collocation values chosen and will examine potential issues or caveats with representing 2016 with only one day in Chapter 5. Lastly, examining 2018 shows the weakest relationships overall, but not far behind 2016 (Figure 4.13). Under the collocation criteria and constraints given in Table 3.2, this data subset contains 27 data points and represents six days of the 2018 campaign.

Perhaps most noticeable in Figure 4.11 is the difference in performance between the two wavelengths. Our hypothesis was for 355 nm BSC and EXT to result in stronger correlations than their 532 nm counterparts due to a shorter wavelength interacting with small CCN aerosols. Results for 2016 show the opposite of this, where 532 nm results for both BSC and EXT are slightly better than 355 nm results (Figure 4.11). On the other hand, 2017 and 2018 results do confirm this hypothesis for BSC, where 355 nm shows a slightly stronger relationship, while EXT shows equal performance between both wavelengths (Figure 4.12 and 4.13, respectively). However, another parameter we consider is relative root mean square error (rRMSE). This is calculated by dividing RMSE by the average of the quantity. By normalizing the

RMSE in this way, comparing values between wavelengths is possible. When looking at these values in addition to R^2, results show that although 355 nm coefficients may have weaker R^2 values, rRMSE is also consistently lower, suggesting that this wavelength does result in less spread in the relationship. Cases where 532 nm is more strongly related to CCN concentration could be due to an increased number of coarse mode aerosols, an issue in collocation averaging, or an error in HSRL-2 observations. This question will be further explored in Sections 4.7 and 5.1.
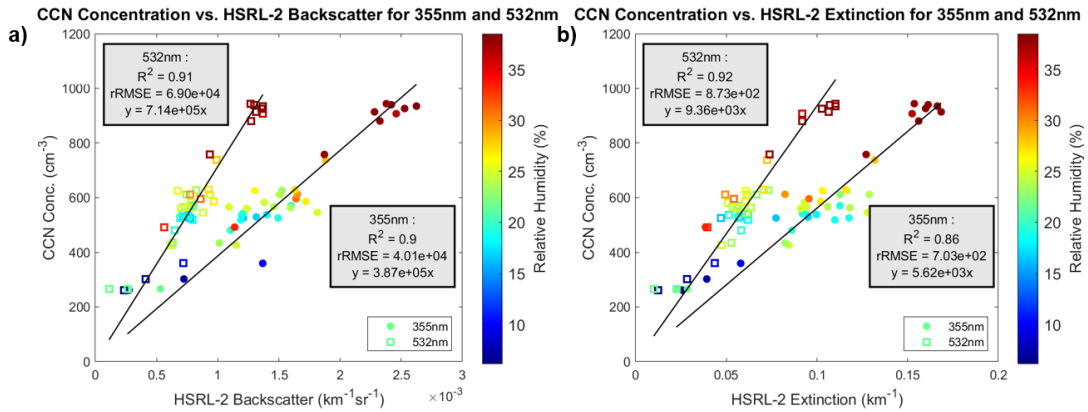
Figure 4.11: 2016 CCN concentration vs. HSRL-2 a) extinction and b) backscatter at both 355 and 532 nm for final collocation criteria, relative humidity, and supersaturation thresholds as given in Table 3.2. Lines of best fit are forced through (0,0) to represent practicality of using linear relationships to quantitatively obtain CCN concentrations using lidar observables.

4.3   CCN vs. Dry Extinction

Although the focus of this study is constraining correlations between in situ CCN concentrations and HSRL-2 BSC and EXT coefficients, we will briefly investigate the relationships between CCN and two additional variables. One of these is in situ dry extinction, measured by the HiGEAR PSAP and nephelometers. Dry extinction is
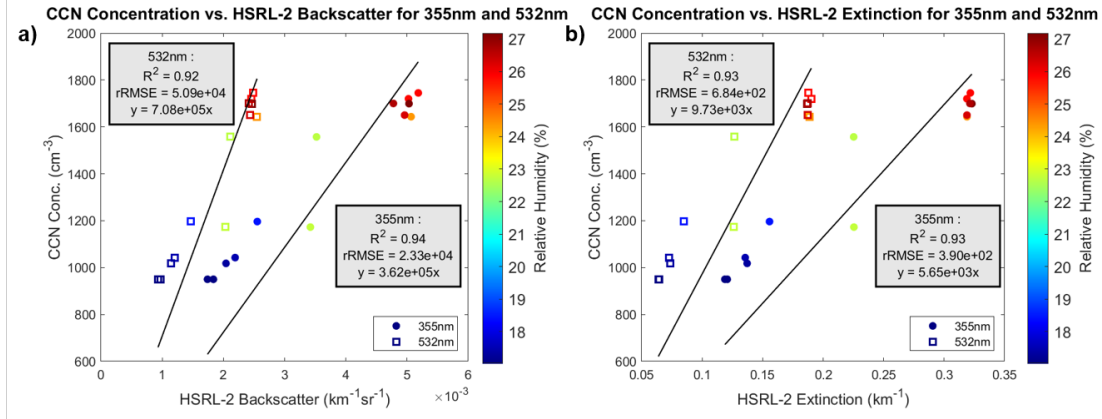
Figure 4.12: 2017 CCN concentration vs. HSRL-2 a) extinction and b) backscatter at both 355 and 532 nm for final collocation criteria, relative humidity, and supersaturation thresholds as given in Table 3.2. Lines of best fit are forced through (0,0) to represent practicality of using linear relationships to quantitatively obtain CCN concentrations using lidar observables.
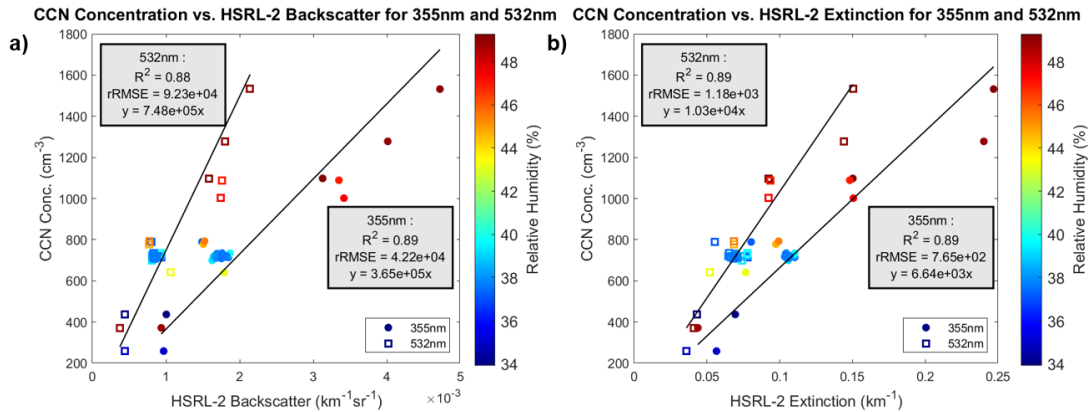
Figure 4.13: 2018 CCN concentration vs. HSRL-2 a) extinction and b) backscatter at both 355 and 532 nm for final collocation criteria, relative humidity, and supersaturation thresholds as given in Table 3.2. Lines of best fit are forced through (0,0) to represent practicality of using linear relationships to quantitatively obtain CCN concentrations using lidar observables.

measured from the same airmass as CCN concentration, and its measurements are not impacted by ambient RH. It is reported at three wavelengths - 450, 550, and 700 nm. These are interpolated to HSRL-2 wavelengths to directly compare results. First, we can examine the differences between the CCN vs. HSRL-2 EXT relationship and

the CCN vs. dry extinction relationship from the dataset determined by our finalized set of collocation criteria. After this we will also look at the entire CCN and dry extinction datasets, not constrained by collocation with the HSRL-2.

When including dry extinction in the CCN and HSRL-2 collocation process, using the finalized collocation criteria, RH, and SS thresholds of Table 3.2, only 2016 and 2018 result in average dry extinction values available to directly compare to HSRL-2 ambient extinction. Results are shown in Figures 4.14 and 4.15 for 2016 due 2018, respectively, and show that similar relationships are formed between CCN concentration and dry extinction as seen using HSRL-2 EXT. Though the slopes of both relationships are comparable, correlation is much weaker for dry extinction. This could be an issue due to sampling volume and aerosol size cutoff of the PSAP and nephelometer or may also be an issue with collocation averaging since these collocation criteria were designed specifically for the CCN vs. HSRL-2 relationship. If the goal were to maximize the CCN vs. dry extinction relationship, the collocation criteria and data filtering steps may have come to different conclusions. However, our main purpose in this step is to explore other variables available in the dataset and compare their performance to what is possible using HSRL-2 BSC and EXT.

Another approach to investigating a CCN vs. dry extinction relationship is to only filter the data by RH and SS, skipping the data collocation step completely. In this way, we look at a similar subset of data in terms of ambient RH and CCN counter SS but are not limited by HSRL-2 data availability. Results for this approach are shown in Figures 4.16 to 4.18 for 2016, 2017, and 2018, respectively. Due to the large amount of data available with this method, results here are shown as a grid

53
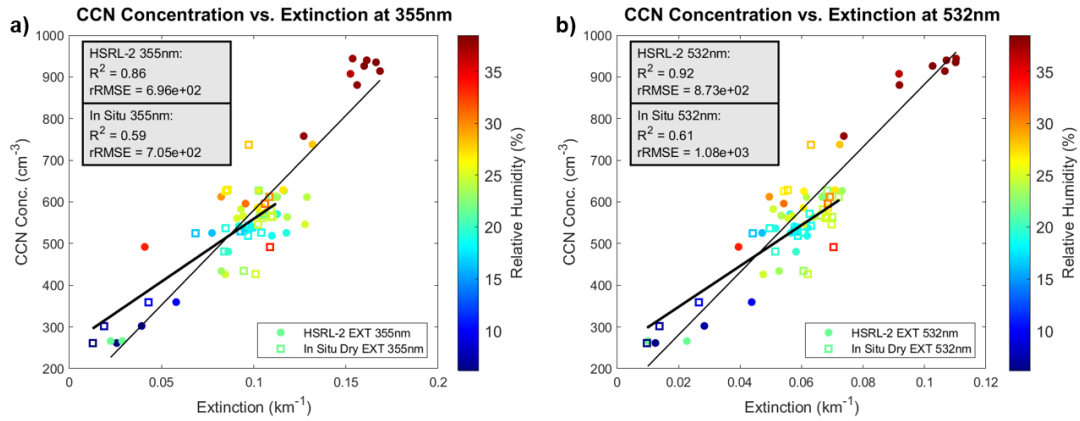
Figure 4.14: 2016 CCN concentration vs. HSRL-2 ambient extinction (circles) and in situ dry extinction (squares) for the final collocated dataset. The longer, solid line corresponds to CCN vs. HSRL-2 extinction, and the shorter, darker line corresponds CCN vs. dry extinction.
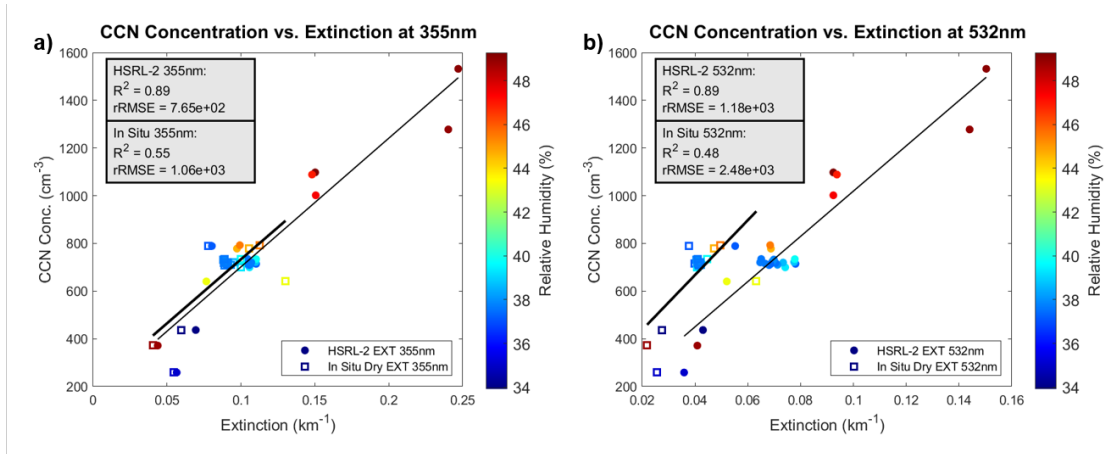
Figure 4.15: 2018 CCN concentration vs. HSRL-2 ambient extinction (circles) and in situ dry extinction (squares) for the final collocated dataset. The longer, solid line corresponds to CCN vs. HSRL-2 extinction, and the shorter, darker line corresponds CCN vs. dry extinction.

color-coded by the number of data points within each grid box. Grid boxes span 0.005 km^{-1} in the x-direction and 50 cm^{-3} in the y-direction. Looking at the data in this manner allows for confirmation that most data lie around the line of best fit, specifically at very low CCN concentration and dry extinction values.

Overall, these results show stronger correlation with CCN concentration than those shown in Figures 4.14 and 4.15 and are more comparable to results from HSRL-2 ambient EXT (Figures 4.16 to 4.18). Only constraining the data by RH and SS results in 6348 points over 4 days for 2016, 3197 points over 6 days for 2017, and 14631 points over 12 days for 2018. 2017 has the most sporadic data availability and lowest total number of dry extinction measurements, perhaps explaining why correlations are weakest for this year compared to the others (Figure 4.17). All dry extinction analysis, whether collocated with HSRL-2 or not, supports the idea that although similar relationships can be drawn between CCN concentration and dry extinction, this method is not necessarily preferable to results obtained using HSRL-2 ambient BSC and EXT.
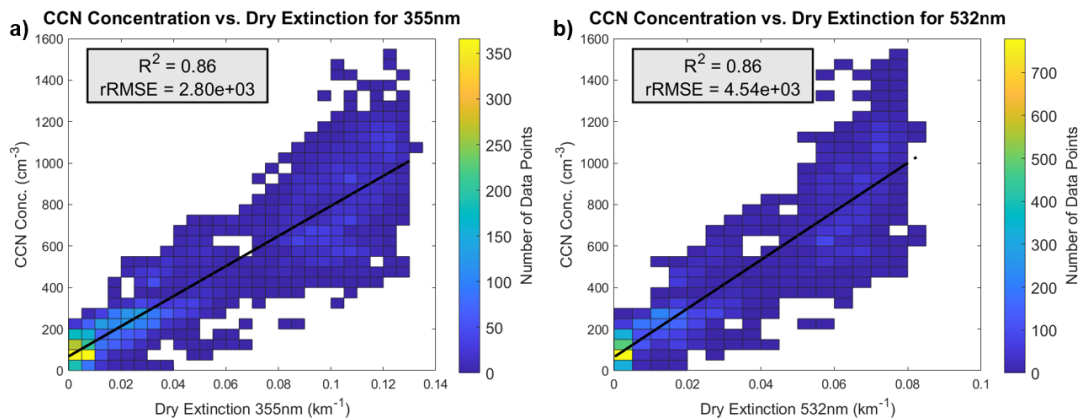
Figure 4.16: CCN concentration vs. in situ dry extinction (squares) for the entire 2016 dataset filtered only by RH$\leq$40% and SS=0.3%. Number of data points (shaded) calculated for grid boxes that span 0.005 km^{-1} in the x-direction and 50 cm^{-3} in the y-direction.
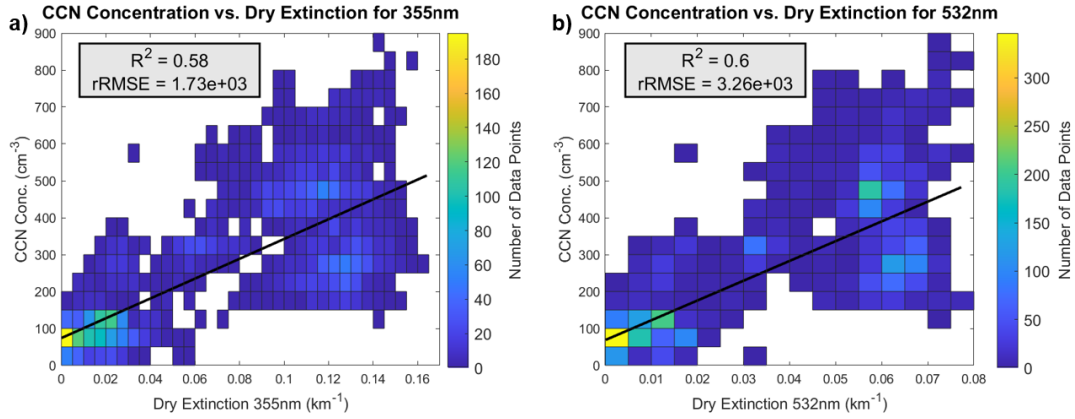
Figure 4.17: CCN concentration vs. in situ dry extinction (squares) for the entire 2017 dataset filtered only by RH≤40% and SS≥0.2%. Number of data points (shaded) calculated for grid boxes that span 0.005 km^{-1} in the x-direction and 50 cm^{-3} in the y-direction.
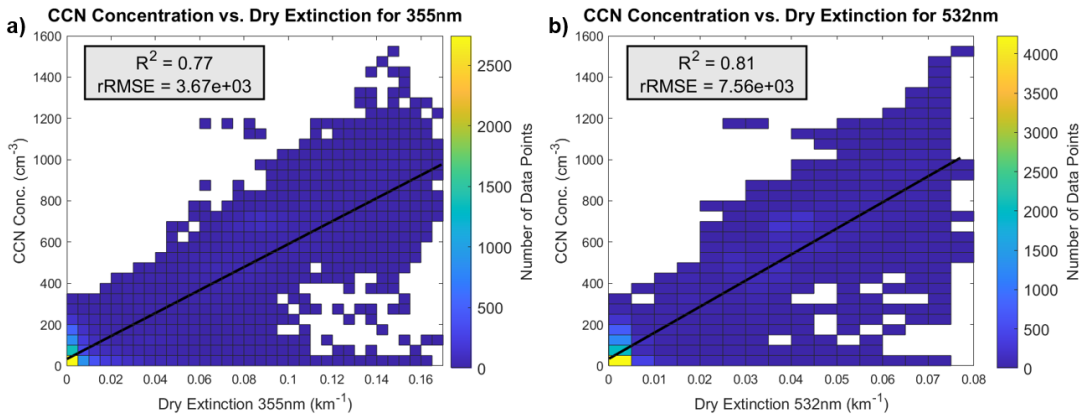
Figure 4.18: CCN concentration vs. in situ dry extinction (squares) for the entire 2018 dataset filtered only by RH≤50% and SS≤0.4%. Number of data points (shaded) calculated for grid boxes that span 0.005 km^{-1} in the x-direction and 50 cm^{-3} in the y-direction.

4.4   CCN vs. Aerosol Index

Another variable that can be compared to CCN concentration is aerosol index (AI), the product of the angstrom exponent (α) and EXT. This is a parameter that is typically thought to represent concentrations of small particles better than other

56

optical properties due to the angstrom exponent being a first indication of particle size (Breon 2002; Liu et al. 2007). Unlike dry extinction, this does not require the use of a separate dataset, but instead utilizes HSRL-2 dry extinction in a new way. To calculate AI we first calculate the angstrom exponent (Eqn. 4.1), and then multiply this by EXT at both wavelengths, resulting in an AI value for 355 nm and one for 532 nm (Eqn. 4.2). This calculation is performed for each individual HSRL-2 observation and values shown in the results are averages resulting from our data collocation process. Once again, these data are collocated and filtered using the values given in Table 3.2.

$$\alpha = \frac{ln[EXT(\lambda_1)/EXT(\lambda_2)]}{ln(\lambda_1/\lambda_2)} \qquad (4.1)$$

$$AI = \alpha * EXT \qquad (4.2)$$

Results for CCN concentration compared with AI are shown in Figures 4.19 to 4.21 for 2016, 2017, and 2018, respectively. Overall, these communicate a result like what is seen in the dry extinction analyses. Use of AI instead of HSRL-2 BSC and EXT yields similar linear relationships with overall weaker correlations. Unlike previous analyses, however, the relationship shown for the 2016 collocated dataset appears weaker and more scattered than 2017 and 2018 while the two latter years appear to have comparable correlation when compared to their CCN vs. HSRL-2 counterparts shown in Figures 4.12 and 4.13. Since AI typically gives an indication of aerosol size, specifically representation of smaller aerosols, it could be that CCN measured in 2016

are larger than expected. This year also represents a smaller range of AI index values, which allows for increased noise in the relationship. Nevertheless, as concluded for dry extinction, although this variable can be related to CCN concentration, it is not necessarily preferable to using HSRL-2 BSC and EXT coefficients.
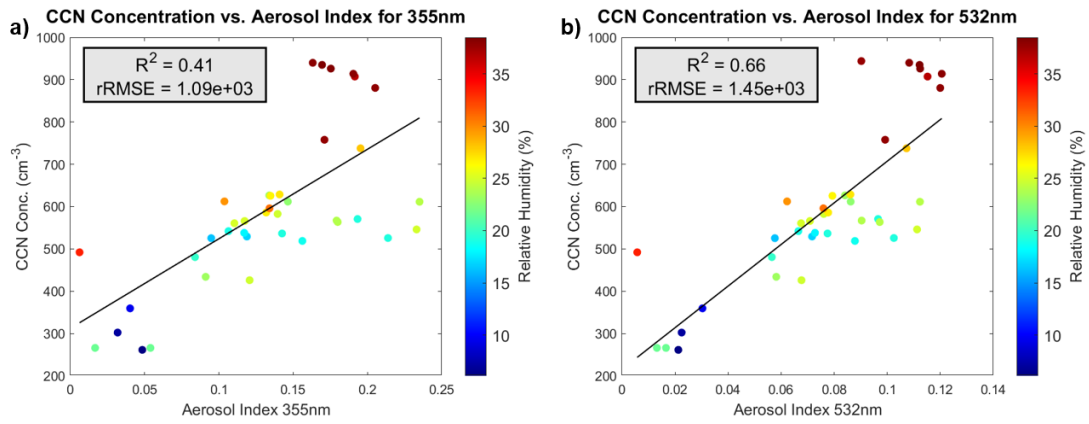
Figure 4.19: 2016 CCN concentration vs. AI for the final collocated dataset.
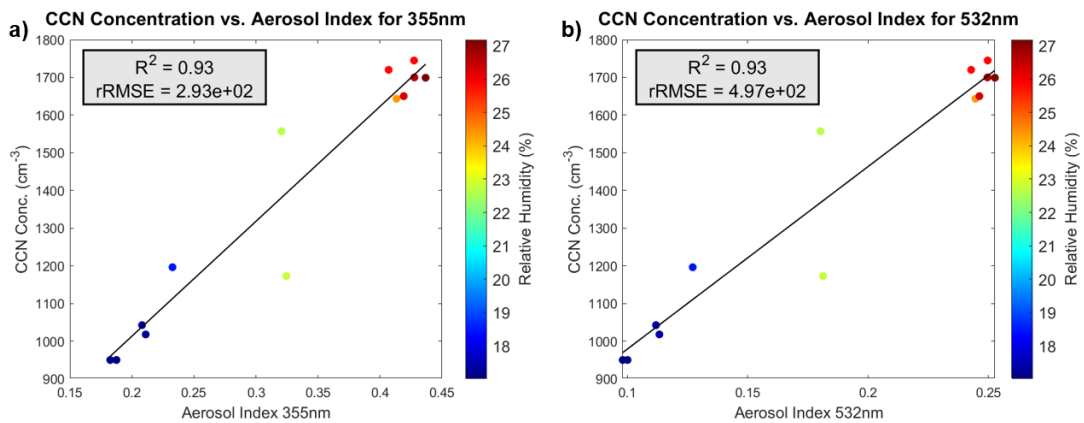
Figure 4.20: 2017 CCN concentration vs. AI for the final collocated dataset.

58
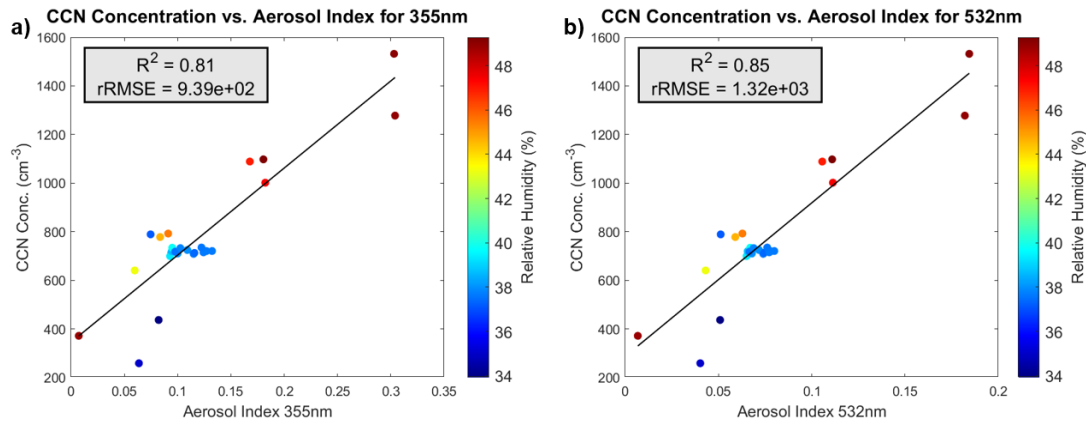
Figure 4.21: 2018 CCN concentration vs. AI for the final collocated dataset.

4.5 Theoretical Optics Closure

As referenced in Section 3.4, a final step of this analysis will use Mie scattering theory to calculate backscatter and extinction coefficients from size distribution parameters and aerosol type specific refractive indices. This analysis will focus on the separate contributions to total backscatter and extinction from fine and coarse mode aerosols. When comparing CCN concentration to HSRL-2 measured optics, we compare fine mode aerosols to observed optics from both modes. Therefore, we are interested in demonstrating that both size distribution modes contribute to observed optics, but not to CCN concentration. This section will present a case study comparison between results achieved using combined lidar and polarimeter retrievals from Xu et al. (2021) to those achieved using in situ measured size distributions for the ORACLES 2016 collocated dataset. Following this, results based on in situ size distributions from 2017 and 2018 will be presented.

4.5.1 Theoretical Optics Case Study Comparison: ORACLES 2016

Figure 4.22 shows a comparison of HSRL-2 measured and Mie theory calculated backscatter and extinction at 355 and 532 nm using aerosol microphysics retrieved from combined lidar and polarimeter observations (Xu et al. 2021). In general, these results show that calculated values compare well to those observed by HSRL-2, and differences fall within measurement uncertainties.
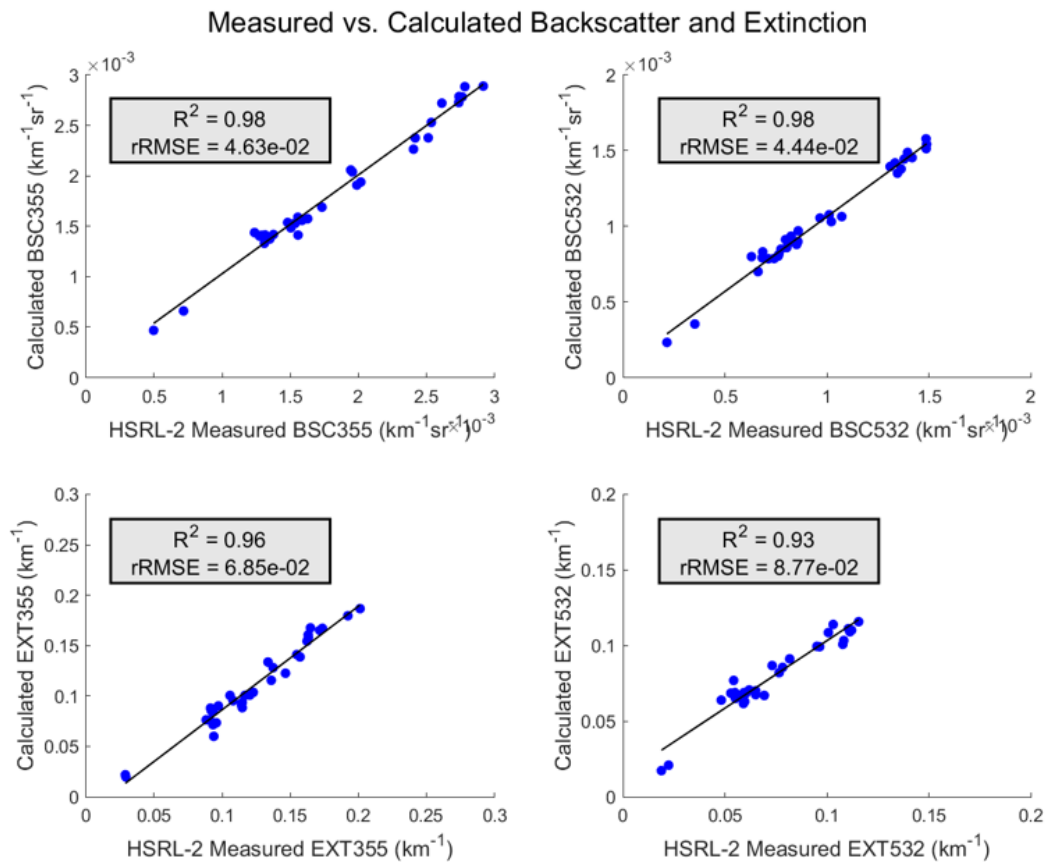
Figure 4.22: Measured vs. calculated backscatter and extinction coefficients for 20160912 flight leg using lidar polarimeter combined retrieval size distributions.

Figures 4.23 and 4.24 show a comparison between in situ CCN measured during the same time (a flight leg measured during the 14 UTC hour) that retrieval data are available and calculated backscatter and extinction, respectively. Since a bimodal size distribution is assumed for aerosols in this region, calculated backscatter and extinction coefficients can be shown for each size mode along with the total value. With these results we are interested in seeing whether theoretically calculated optics show stronger correlation with CCN at the 355 nm wavelengths, and in quantifying the contribution of a coarse mode that may weaken the relationship between CCN concentration and HSRL-2 measured BSC and EXT. Both figures show coarse mode calculated backscatter and extinction contributing positively toward total coefficient values. Additionally, CCN concentration has a stronger relationship with fine mode backscatter and extinction at 355 nm than at 532 nm, supporting the idea that smaller aerosols would be better represented at shorter wavelengths. However, the total calculated coefficients do not necessarily show the same pattern, suggesting that the presence of coarse mode aerosols does impact results and the validity of our initial hypothesis.

Before proceeding to theoretical optics results using collocated, in situ size distributions, it is important to reiterate that the major difference expected when comparing results from retrieval data to those from in situ data is related to accuracy of the size distributions. More specifically, the retrieval algorithm updates and adjusts size distributions dynamically, resulting in more reliable data, such as a better represented coarse mode. On the other hand, errors and noise more likely to be found in *in situ* measured size distributions will carry through the entire calculation process. Coarse

Figure 4.23: In situ CCN concentration vs. fine mode, coarse mode, and total backscatter coefficients for 20160912 flight leg calculated using lidar polarimeter combined retrieval size distributions.

Figure 4.24: In situ CCN concentration vs. fine mode, coarse mode, and total extinction coefficients for 20160912 flight leg calculated using lidar polarimeter combined retrieval size distributions.

mode tends to be underrepresented in *in situ* measurements, which proves to be problematic in calculations of r_m and σ_g, where size is an especially important parameter

(Equations (3.1) to (3.5)). Another inherent difference between these methods is that in situ size distribution measurements are made at dry conditions, while retrieval data represents the ambient condition. Lastly, if in situ size distributions are measured in a gap region where aerosol concentrations are low, a lognormal distribution may not fit the data well, causing additional errors in calculating input values to the Mie scattering equations.

With these caveats in mind, Figures 4.25 and 4.26 show a similar breakdown as given in Figures 4.23 and 4.24 with collocated CCN measurements compared to calculated backscatter and extinction, respectively. These CCN concentration and in situ size distribution measurements are from the same leg represented in results using retrieval data. Like retrieval-based results, these also show a strong relationship between fine mode backscatter and extinction with CCN concentration and a weaker relationship with coarse mode calculated coefficients. In general, the coarse mode appears to have a weaker and lower magnitude contribution, which could suggest an underestimation of coarse mode aerosol concentrations by the in situ measurements or an underestimation by the combined lidar+polarimeter retrieved size distributions. Regardless, calculations made using in situ size distributions do support the hypothesis that backscatter and extinction at 355 nm correlate more strongly with CCN concentration values than their 532 nm counterparts. These calculations also more clearly show a breakdown in the relationship between CCN and total backscatter and extinction due to contributions by coarse mode aerosols.

Figure 4.25: 2016 in situ CCN concentration vs. fine mode, coarse mode, and total backscatter coefficients calculated using in situ collocated size distributions.
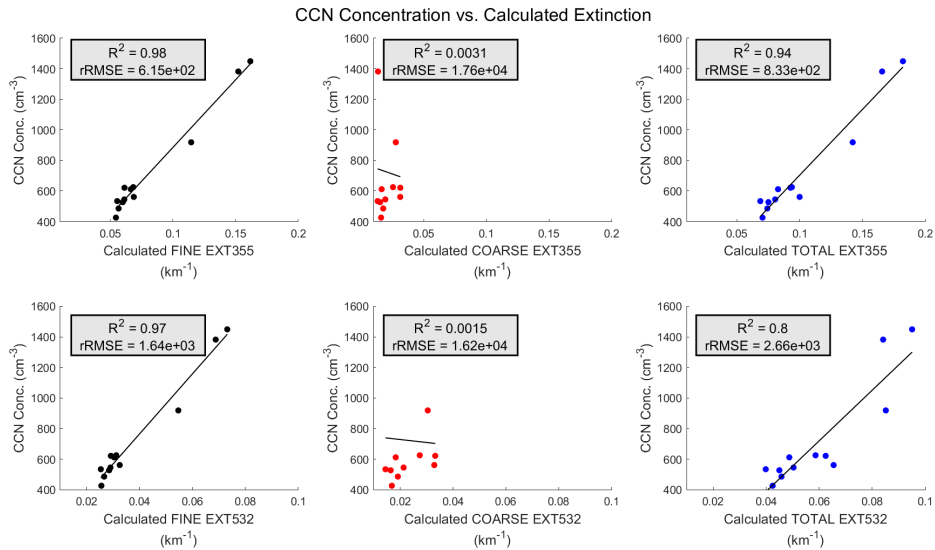
Figure 4.26: 2016 in situ CCN concentration vs. fine mode, coarse mode, and total extinction coefficients calculated using in situ collocated size distributions.

4.5.2 Theoretical Optics: ORACLES 2017 and 2018

Without combined lidar+polarimeter retrieval data available for ORACLES 2017 and 2018, this section will look at results for theoretical optics calculations using in

situ size distributions and the same refractive index values as used for 2016 (Table 3.3). It is important to keep in mind that due to having smaller collocated datasets for 2017 and 2018, these calculations are also limited by fewer data points than 2016. Figures 4.27 and 4.28 show 2017 collocated CCN concentration compared to calculated backscatter and extinction, respectively. Unlike 2016, coarse mode backscatter and extinction contributions are higher in magnitude. This may be related to differences in sampling region, since flights further north during 2017 and 2018 observed dust particles more often than in 2016. Larger dust particles may cause an increase in coarse mode optics. Nevertheless, fine mode backscatter and extinction continue to be more strongly correlated with CCN concentration, while coarse mode weakens the relationship with total coefficients. Additionally, a clear difference in performance between total backscatter and extinction is seen between wavelengths, with 355 nm generally resulting in a stronger correlation.

Figures 4.29 and 4.30 show the equivalent analyses for 2018 and the patterns and results generally follow what is seen in 2016 and 2017. In summary, Mie theory calculations of theoretical backscatter and extinction coefficients based on in situ size distributions allow us to separate out contribution to total backscatter and extinction from fine and coarse mode aerosols. While CCN are primarily fine mode aerosols, HSRL-2 observed optics represent contributions from both modes. Therefore, this analysis allows us to see that those relationships between CCN concentration and backscatter and extinction coefficients as calculated from fine mode contributions are usually strongest, and that contributions from the coarse mode weaken the relationship with total backscatter and extinction. However, despite this weakening, total

calculated backscatter and extinction at 355 nm are more strongly correlated with CCN concentration than at 532 nm, as our hypothesis stated.
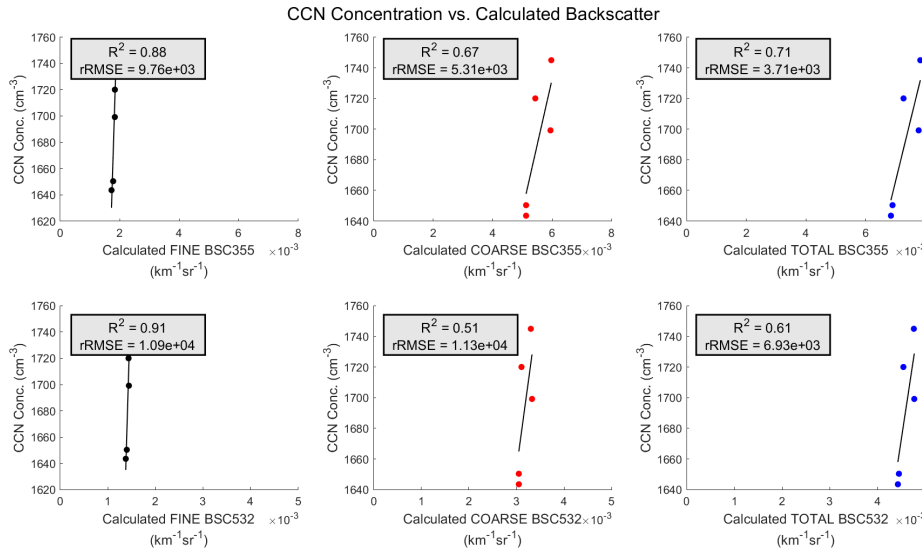
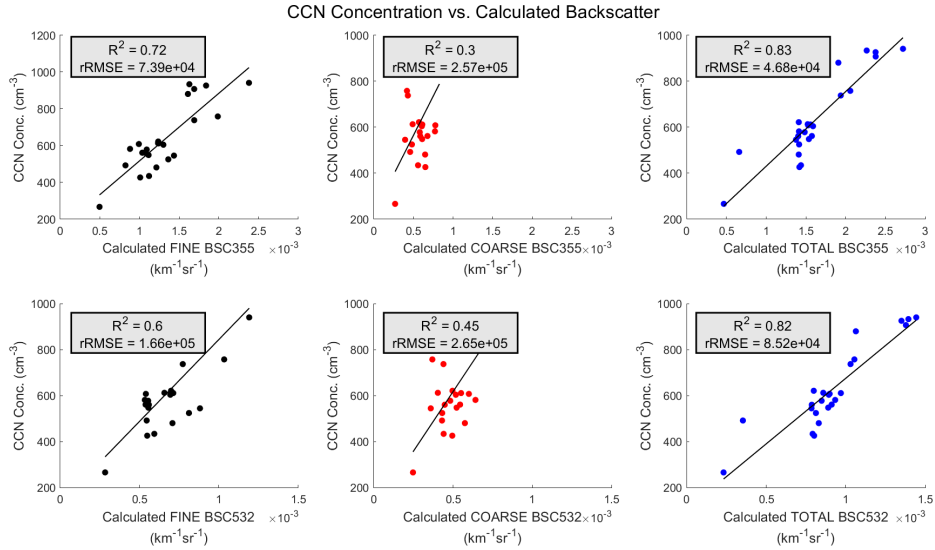
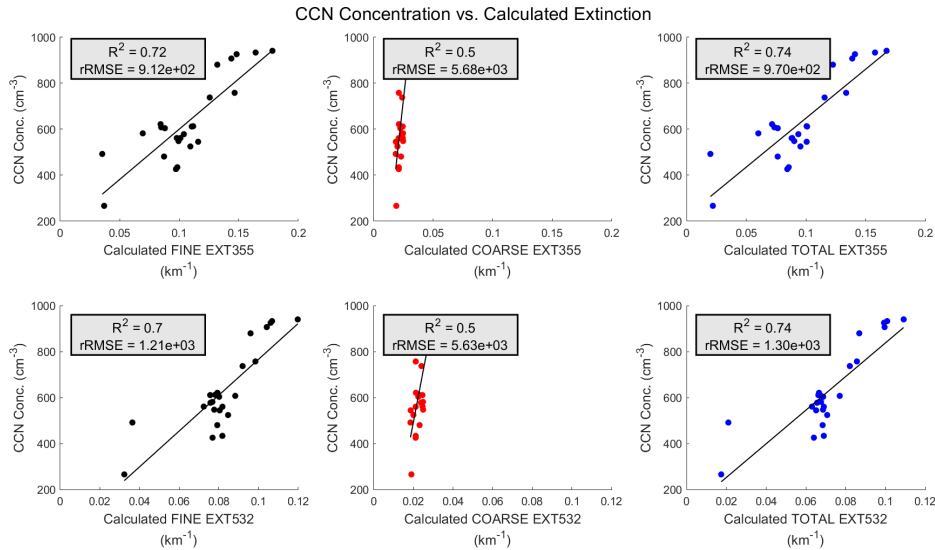Figure 4.27: 2017 in situ CCN concentration vs. fine mode, coarse mode, and total backscatter coefficients calculated using in situ collocated size distributions.
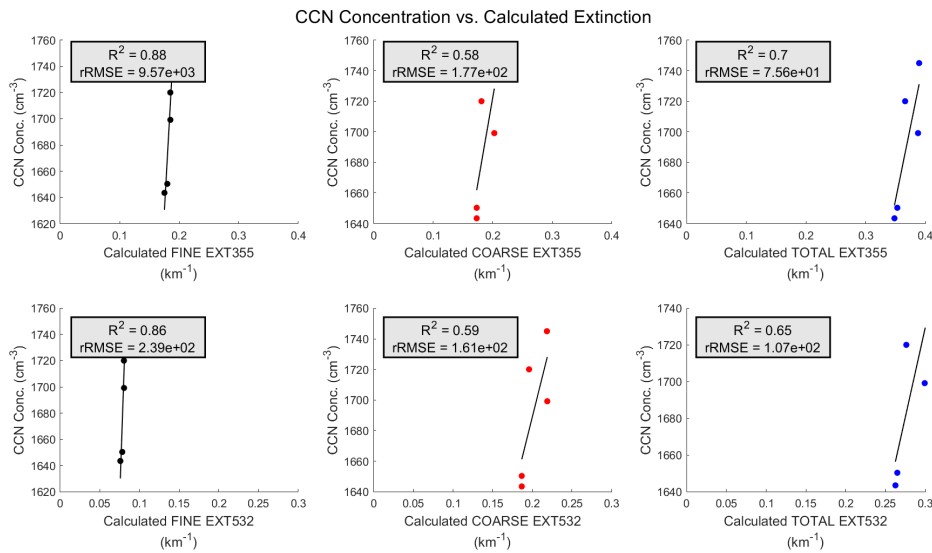
Figure 4.28: 2017 in situ CCN concentration vs. fine mode, coarse mode, and total extinction coefficients calculated using in situ collocated size distributions.
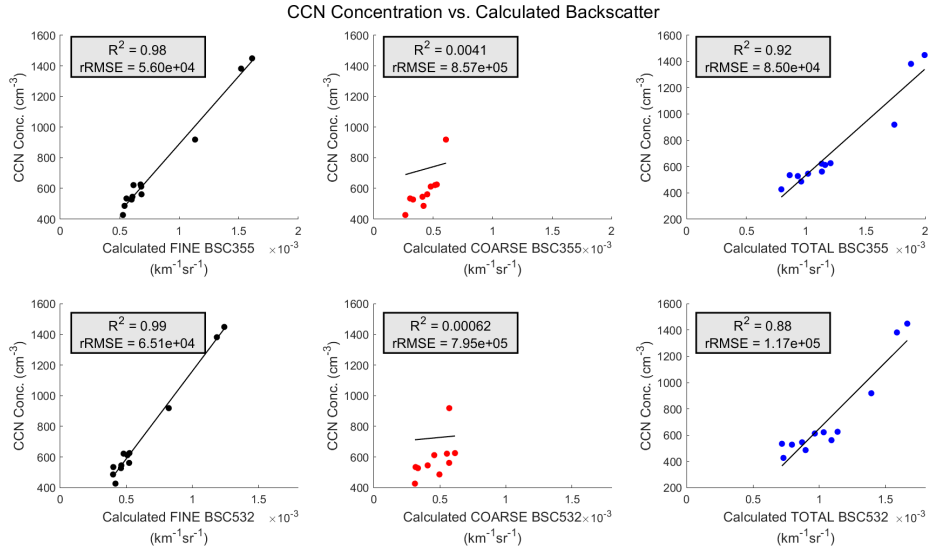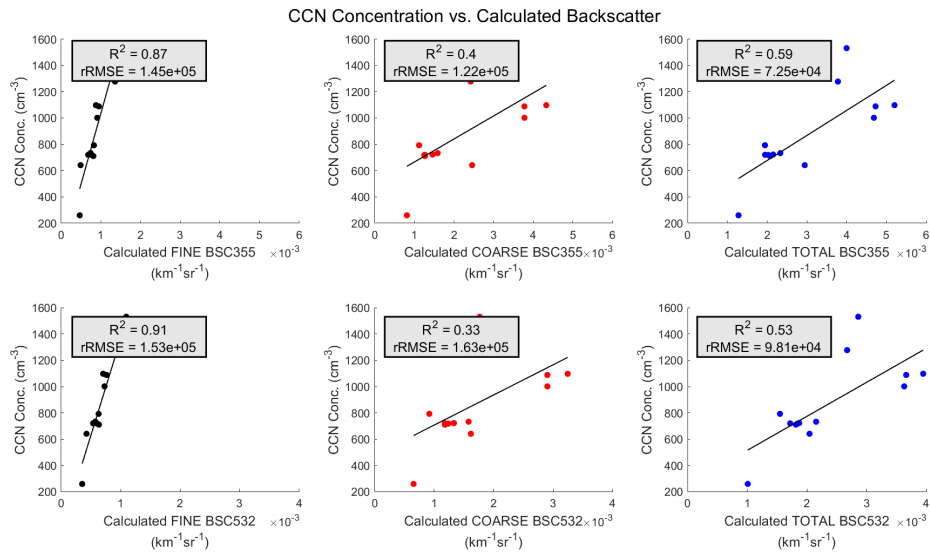
Figure 4.29: 2018 in situ CCN concentration vs. fine mode, coarse mode, and total backscatter coefficients calculated using in situ collocated size distributions.
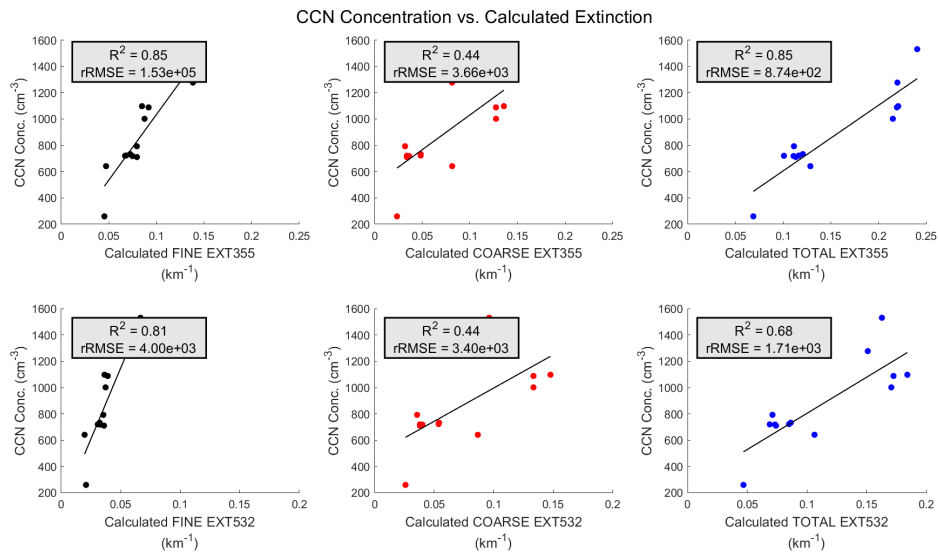
Figure 4.30: 2018 in situ CCN concentration vs. fine mode, coarse mode, and total extinction coefficients calculated using in situ collocated size distributions.

Chapter 5

Discussion

Chapter 4 presented an in-depth look at how CCN and HSRL-2 datasets are collocated before analysis, including sensitivity testing of horizontal, vertical, and time thresholds. It also explored implications of different RH and SS thresholds, as well as how CCN concentration can also be compared to dry extinction and AI. This chapter seeks to understand why CCN vs. HSRL-2 relationships may be stronger for some years than others and further addresses our initial hypothesis that 355 nm coefficients would result in stronger relationships compared to their 532 nm counterparts. It will also address possible sources of error, specifically in the collocation averaging technique and Mie scattering calculations, and conclude with a step back to consider the large-scale implications and applications of this work.

5.1 Inter-year and Inter-wavelength Differences

5.1.1 Location and Aerosol Age

When comparing results from three separate years of observations, it is important to recognize inherent environmental differences. One major difference between the three years of this campaign is that observations were made during different parts of the seasonal biomass burning cycle (Redemann et al. 2021). Therefore, there are likely

differences in the exact type of material being burned, as well as age of observed aerosols. Secondly, observations were made in different regions of the SEA each year. While Figure 2.2 shows the different flight paths, Figure 5.1 indicates where the final, collocated data points were measured. While 2016 data are restricted to the southeastern part of the domain, 2017 and 2018 reach further north and west. Figure 5.2 shows a simplified schematic of a commonly occurring trajectory for BBA ejected westward that later descend into the boundary layer (Redemann et al. 2021). When comparing this pathway to Figure 5.1, we could infer that data observed for 2016 is likely dominated by older aerosols that have possibly begun descent into the boundary layer. On the other hand, most data from 2017 and 2018, especially those located further north, were likely measured closer to the time they were ejected from the smoke plume.

Age of any given parcel impacts, among other properties, the chemical composition of aerosols. This can be further explored using measurements of f44, the mass-to-charge ratio m/z 44 relative to total organics. Higher values indicate increased amounts of carboxylic acids and imply that measured aerosols are relatively old (Redemann et al. 2021). Figure 5.3 shows CCN concentration vs. HSRL-2 EXT at 355 nm and final collocation criteria for 2016, 2017, and 2018 at points where f44 data is available. In general, 2017 and 2018 show much lower average f44 values, with both 2017 points having an average of 0.17 and 2018 values ranging from 0.19-0.21. Most data in 2016 also have low f44 values, but a few higher valued points increase the f44 range to 0.2-0.58. Like what was hypothesized from their locations in Figure 5.2, the presence of a few high f44 values in 2016 suggests that some measured aerosols are
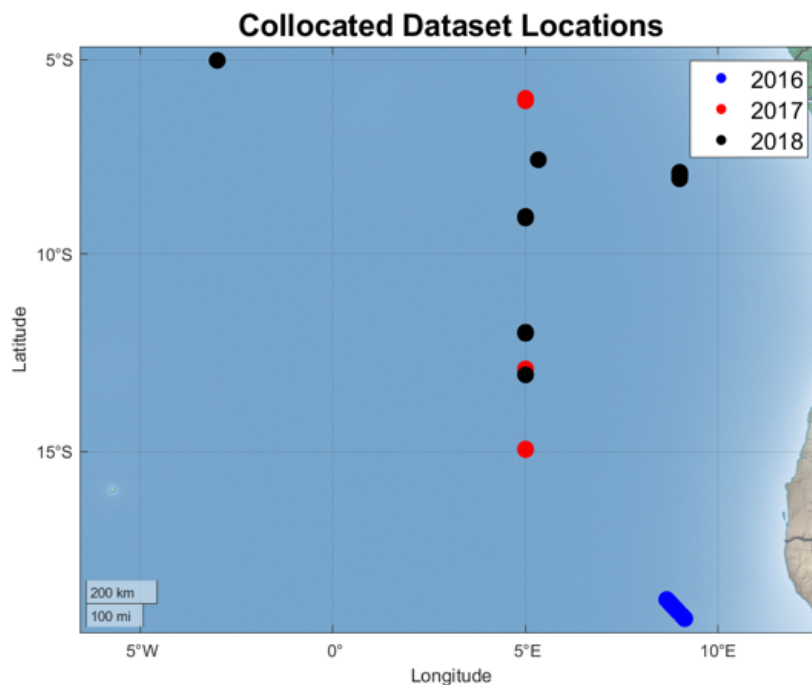
Figure 5.1: Location of collocated data points for each year relative to each other and relative proximity to the coast. While 2016 data are in the southeastern part of the domain, 2017 and 2018 are sampled further north and west.

likely older than what is measured in the other two years. Nevertheless, it is encouraging that despite a few higher f44 values observed in 2016, we seem to be analyzing very similarly aged aerosols overall. This serves as one source of validation for our forthcoming efforts to look at CCN vs. HSRL-2 results for the combined three year data set.

Beyond these interannual differences, we are interested in understanding the limitations in correlation between CCN concentration and observed optical properties - is a lack of correlation due to spatial and temporal variability of CCN, or another

Figure 5.2: Figure from Redemann et al. (2021) shows an example of a commonly occurring pathway for smoke aerosols that are lofted and advected westward and later proceed to descend in into the marine boundary layer.

factor? The next three sections will try to answer this question using standard deviations resultant from the collocation averaging technique, CCN autocorrelation, and results from theoretically calculated optics.

5.1.2 Collocation Averaging

One aspect of the methodology with potential to negatively impact correlation is the collocation averaging. Section 4.1.3 explored the impacts of different horizontal, vertical, and time criteria. However, we have not yet examined possible errors or correlation differences due to averaging. This section will compare standard deviation of CCN concentration within collocated points to see if weaker correlation between years might be due to outliers negatively impacting the collocation averaging.

Figure 5.3: CCN concentration vs. HSRL-2 EXT at 355 nm for 2016 (circles), 2017 (squares), and 2018 (diamonds) collocated datasets. Scatter points are colored by f44 value. These values range from 0.2-0.58 for 2016, 0.17 for 2017, and 0.19-0.21 for 2018. Number of data points is lower than what has been seen when using collocated data sets due to missing f44 values. Lines of best fit are forced through (0,0) to represent practicality of using linear relationships to quantitatively obtain CCN concentrations using lidar observables.

Figure 5.4 shows CCN concentration versus EXT at 355 nm for 2016, 2017, and 2018. For simplicity only one coefficient is shown since all four communicate the same key point. From previous analysis 2017 relationships have shown the strongest correlation overall (Figure 4.12). Results for 2016 are slightly weaker, and 2018 shows the weakest correlation overall (Figures 4.11, 4.13). A very similar trend can be found in CCN standard deviation values. For example, while 2017 has the largest range of CCN standard deviation, only one outlier point (circled) corresponds to the higher end of this range while the other collocated data points correspond to very low standard

deviations. 2016 has the smallest range of CCN standard deviation, but an increased number of points with higher values. 2018 has a range falling between the other years, but again, there are more points that display relatively high values when compared to 2017. The next section will explore inhomogeneity of CCN in more detail, but CCN standard deviation presented here gives a picture of the possible implications of averaging CCN concentration values of varying homogeneity during collocation.
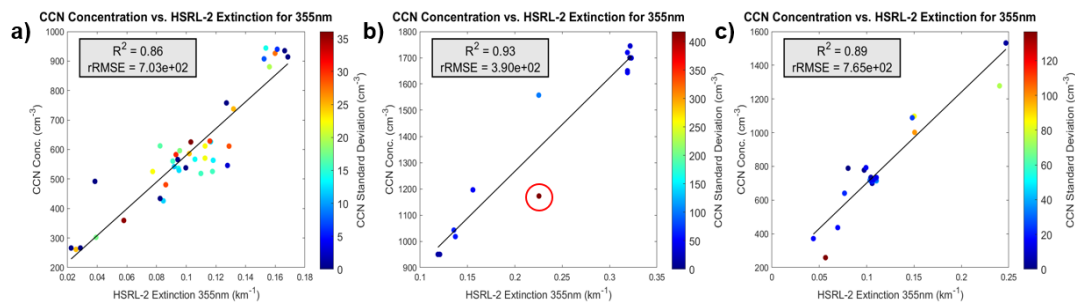
Figure 5.4: CCN vs. HSRL-2 for a) 2016, b) 2017, and c) 2018 collocated datasets with CCN standard deviation within each point indicated by color fill. Note that figure axes are not equivalent between years.

5.1.3   CCN Autocorrelation

Another possible factor impacting correlation is environmental variability of CCN. If CCN concentration is highly heterogeneous over time and space, then averaging values over time and space to correlate with HSRL-2 measurements may not be reliable. While CCN standard deviation within collocated points (Figure 5.4) gives an after-the-fact look at variability within data points that have been already been averaged, we can also look at region-specific CCN concentration variability through autocorrelation.

To begin, Figure 5.5 shows lag-1 CCN concentration compared with the unlagged dataset, with the lag-1 autocorrelation coefficient annotated. All CCN between 3-5 km and measured at the SS values given in Table 3.2 are considered to focus on variability of the smoke plume aerosols. In a study on mesoscale variations of various tropospheric aerosols, Anderson et al. (2003) found that random instrumental noise is usually manifest in lowering of the lag-1 autocorrelation. However, lag-1 autocorrelation coefficients all close to unity indicate that measurement noise and ambient variability at this 1-second resolution are small (Figure 5.5).
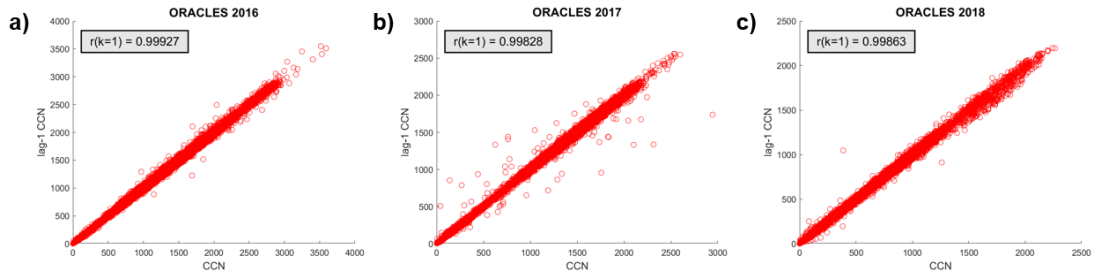
Figure 5.5: Lag-1 autocorrelation coefficients for a) 2016, b) 2017, and c) 2018 CCN concentration datasets. Note that figure axes are not equivalent between years.

Since measurement noise and ambient variability are small, we can move on to look at horizontal variability of CCN in the SEA using autocorrelation, confident that variations are not due to instrument noise. To look at CCN variability as a characteristic of the region, CCN autocorrelation is calculated for a variety of lags using one horizontal leg from each day of ORACLES that is considered in this analysis. Each horizontal leg spans a vertical range of less than 100 m to minimize vertical variability. Results for this analysis are shown in Figure 5.6, where panel (a) shows autocorrelation coefficient as a function of lag, and panel (b) shows the number of data

points included in the analysis at each lag. Autocorrelation of CCN concentration decreases slightly around 100 km, increases again around 400 km, and then drops off rapidly after 600 km and becomes much noisier. The number of data points included in the analysis begins to decrease more rapidly after 600 km as well.
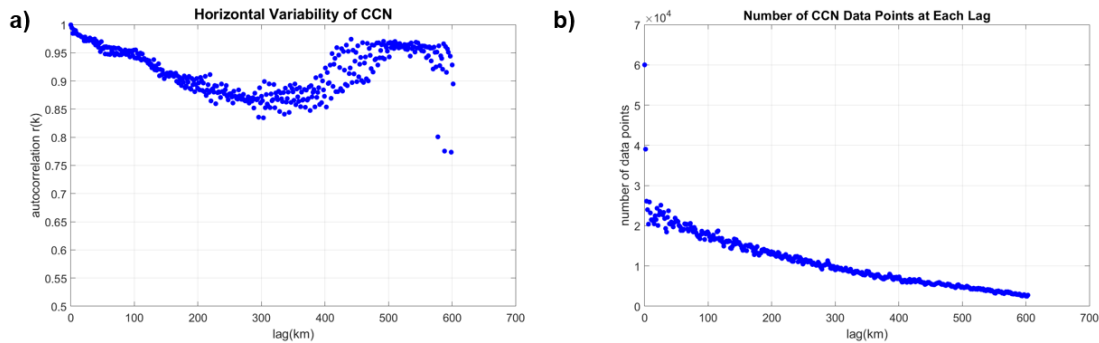
Figure 5.6: For a combination of horizontal flight legs, a) autocorrelation coefficient vs. lag and b) number of data points available vs. lag.

To apply these results more directly to this analysis, CCN autocorrelation between lags of 1 and 30 km are shown in Figure 5.7. The point annotated in the figure represents typical CCN autocorrelation at about 2 km, which corresponds to the horizontal distance with which CCN and HSRL-2 data sets are collocated. At this horizontal distance, the autocorrelation coefficient is 0.9944. Therefore, two main conclusions can be drawn. First, correlation between CCN concentration and HSRL-2 coefficients arguably can only be as strong as CCN is correlated with itself within the same spatiotemporal domains. Therefore, when using a horizontal collocation criterion of 2 km, we can only reasonably expect the relationship to have an R^2 of 0.9944. Secondly, high autocorrelation suggests that averaging within a horizontal distance of 2 km is reasonable for this region. Stepping back to Figure 5.6, results

show that CCN is well correlated with itself for much longer than 2 km. In future studies, it could be possible to collocate CCN at longer time and horizontal distances if including a corresponding horizontal average of HSRL-2 coefficients as well.
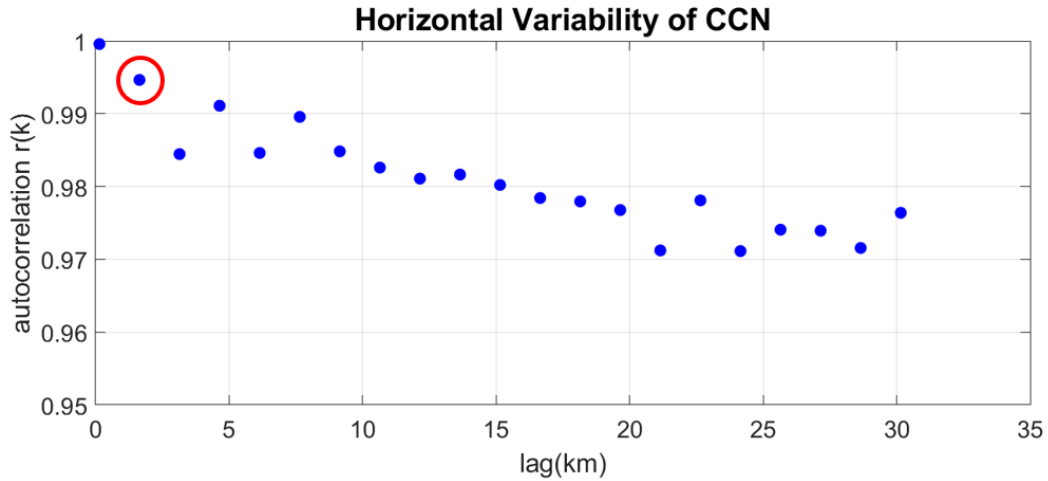
Figure 5.7: Autocorrelation for horizontal flight legs shown for 1 to 30 km.

5.1.4 Theoretical Optics

As seen in the previous three sections, inter-year differences can be explained in part by factors such as aerosol age and location of measurement, as well as variability of CCN averaged together through collocation. While these analyses help explain smaller discrepancies between the three years, a remaining question involves our initial hypothesis about expected wavelength differences. Due to the small size of most CCN, it was hypothesized that 355 nm HSRL-2 BSC and EXT would result in stronger correlations due to a smaller wavelength interacting with smaller aerosols. However, results from comparing in situ CCN concentrations to HSRL-2 coefficients

have not shown this to usually be true. Instead, a few cases showed 532 nm coefficients correlating more strongly with CCN concentration while others showed nearly equal performance by both (Figures 4.11 to 4.13).

To investigate why this may be the case, Mie scattering theory was used to calculate theoretical backscatter and extinction coefficients. Calculations done using lidar+polarimeter retrieved size distributions available for 2016 resulted in stronger relationships between CCN concentration and fine mode backscatter and extinction at 355 nm than at 532 nm but results for total backscatter and extinction remained relatively equal (Figures 4.23 and 4.24). On the other hand, calculations done using in situ size distributions, as shown in Figures 4.25 to 4.30, all show total coefficients at 355 nm correlated more strongly with CCN concentration than their 532 nm counterparts.

It would be unrealistic to draw a conclusion between in situ and retrieved size distribution performance since results can only be compared for 2016. Retrieval size distributions are speculated to be more accurate due to dynamic updates to size distributions and refractive indices (Xu et al. 2021), while in situ size distributions can tend to misrepresent coarse mode concentration of aerosols. Furthermore, the dry nature of in situ measurements compared to ambient conditions for retrieved size distributions can impact sizing differences. Nevertheless, one similarity in their results is the stronger relationship between CCN concentration with 355 nm calculated fine mode optics as opposed to 532 nm calculated fine mode optics. Overall, theoretical optics calculations seem to support the idea that in most cases 355 nm coefficients,

77

with contributions from the entire size distribution, should have a stronger relationship with CCN concentration than 532 nm results. The fact that this is not the case in many of the observations could be due to an issue with HSRL-2 channel accuracy, calibration, or other instrument issues and would be an interesting area for future, more in-depth study.

5.2   Broad Implications

Most analysis until now has looked at one year of data at a time. However, if we are interested in characterizing CCN concentrations over the SEA with a method that should theoretically hold at any time for a BBA dominated environment, it is important to also compare relationships between all years. If correlations vary wildly between different years and locations of observation, then the goal of using remotely sensed optics to infer vertically resolved CCN concentration would not be feasible. Figure 5.8 presents results for each coefficient, with each years' collocated data shown together. The best fit line slopes for 2016 and 2017 appear most similar for each coefficient. Results for 2017 are most consistently offset from those for 2016 and 2018, where higher CCN concentrations are observed. However, despite these minor differences the similarity between years is encouraging.

When considering the main goal of this study – to develop a relationship with which CCN concentrations can be inferred using HSRL-2 BSC and EXT coefficients – the culmination of all previous sensitivity testing and year-by-year analysis is given by Figure 5.9. Here all data from Figure 5.8 has been combined to fit a relationship
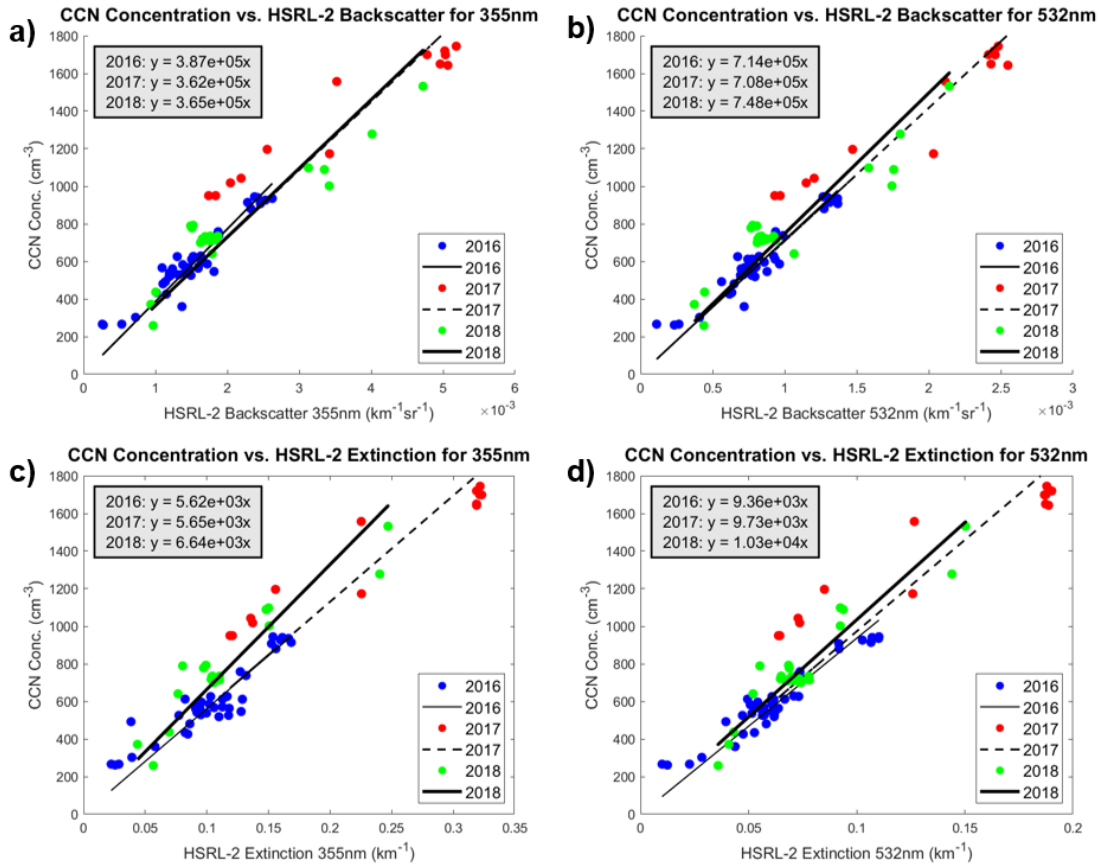
Figure 5.8: CCN concentration vs. each HSRL-2 coefficient with all years' results shown on each panel. Lines of best fit are forced through (0,0) to represent practicality of using linear relationships to quantitatively obtain CCN concentrations using lidar observables.

between CCN concentration and HSRL-2 BSC and EXT. An initial observation is that results from each separate year, as indicated in Figure 5.8, are similar enough that when fitting the entire three-year dataset, correlation remains relatively high. Across 2016, 2017, and 2018 this complete dataset is represented by 80 total data points spanning 10 days (for each coefficient). Like previous analyses, the 355 nm coefficients do not result in noticeably higher correlations than 532 nm. In this case R^2 coefficients are equal at both wavelengths, and BSC shows a slightly stronger correlation than EXT.
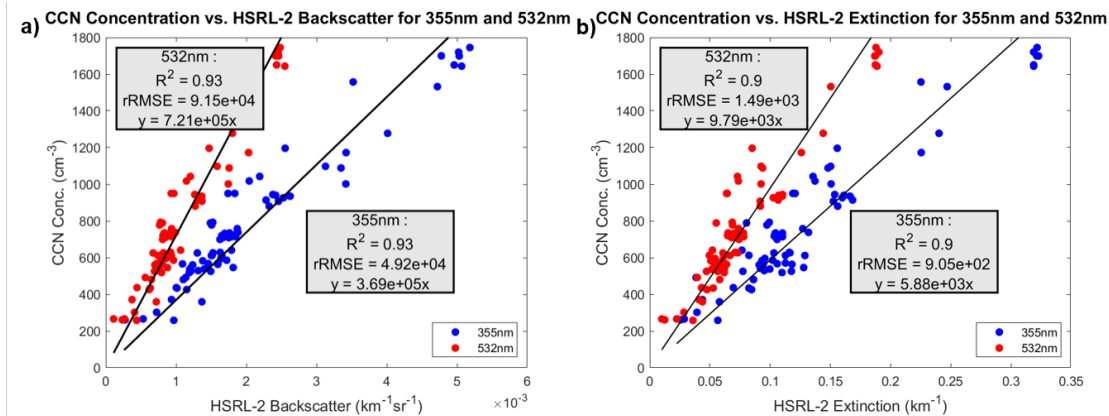
Figure 5.9: CCN concentration vs. HSRL-2 backscatter and extinction, with both wavelengths shown on each panel. This combined dataset represents 10 days of measurements and 80 total collocated data points (per coefficient). Lines of best fit are forced through (0,0) to represent practicality of using linear relationships to quantitatively obtain CCN concentrations using lidar observables.

Moving forward, these results suggest significant possibility to estimate CCN concentrations in regions where lidar measurements of extinction and backscatter are available without a need for expensive in situ measurements. Since satellite-borne lidar measurements would be available at more regular time intervals and over larger domains, CCN concentration estimates would be more numerous as well, not limited to specific in situ domains and time ranges. An increased amount of CCN concentration data available will aid in having the resources to better understand and reduce uncertainty related to aerosol-cloud interactions. One important caveat to application of these results is that the relationships drawn here are regime-specific and will only apply to biomass burning aerosols, specifically those over the SEA. Since CCN activation depends strongly on aerosol chemical composition and mixing state, the relationships developed here with HSRL-2 coefficients will vary for different aerosol types. Therefore, while these specific results will not directly apply to every case, the

methodology present should be a realistic place to start when characterizing other regions and aerosol types.

Enabling the understanding of aerosol-cloud interactions and reducing their uncertainty is not an issue limited to BBA in the SEA, despite the importance of both BBA and a semi-permanent stratocumulus deck in this region. Therefore, potential future work could investigate drawing similar relationships between lidar measured backscatter and extinction with CCN concentrations in regions dominated by different aerosol types. Another limitation of this study is its focus on CCN measured in "dry" conditions. This inhibits understanding of CCN concentrations in more humid regions, such as near cloud bases. Therefore, future study could focus on observations made in humid regions. We have showed the impact that hygroscopicity of aerosols can have when combined with observations made at low RH conditions, so it may be necessary to isolate observations made at high RH to correlate with lidar observations in a similar manner.

Additionally, aerosol age and horizontal autocorrelation would likely benefit from more in-depth analysis that was not possible for this study due to time constraints. For example, one limitation to using f44 as an indicator of aerosol age was a lack of complete data availability. Results for 2017 and 2018 were limited to two and four data points with f44 available, respectively (Figure 5.3). This makes it difficult to draw conclusions between each year. In the future it would be interesting to use another, more complete data set, such as model output parameters, to estimate aerosol age and draw a stronger conclusion. Furthermore, horizontal autocorrelation could be expanded and made more conclusive by including more horizontal legs from

each flight in the autocorrelation calculations. In addition to adding more data to the calculations, it would be interesting to further investigate possible explanations for the apparent rebound in autocorrelation that occurs at about 600 km. Understanding why this occurs may expand understanding on horizontal variability of CCN in the SEA over longer periods of time.

Chapter 6

Conclusion

The ORACLES campaign over the Southeast Atlantic observed a seasonal biomass burning smoke plume that is advected westward over a semi-permanent stratocumulus cloud deck. Due to the radiative and microphysical properties of the stratocumulus deck, which acts as a major climate thermostat, and the biomass burning aerosols, that can absorb incoming solar radiation or act as CCN that interact with the stratocumulus deck, this region is of particular interest in terms of radiative forcing and aerosol-cloud interactions. Using lidar aerosol extinction and backscatter coefficients measured with the HSRL-2 and in situ measured CCN concentrations, this study investigates relationships between both variables to explore the possibility of obtaining vertically-resolved CCN concentrations solely using remote sensing techniques. If feasible, aerosol-cloud interaction relevant data would be more widely available in regions without in situ observations. To conclude, each of the four primary science questions outlined in Section 2.4 that motivated this study will be addressed and answered.

SQ (1) asked how CCN number concentration and HSRL-2 observed aerosol optical properties are related in the BBA dominated SEA. Figures 4.11 to 4.13 answer this question by showing the primary results for each year of data as linear relationships between CCN concentration and HSRL-2 BSC and EXT. After data collocation

and filtering, we can draw similar relationships where increasing BSC and EXT are associated with increasing CCN concentration.

SQ (2) expands on SQ (1) in asking how relationships between CCN number concentration and aerosol optical properties are similar for different parts of the seasonal burning cycle. We have addressed this in terms of location and time of measurement through both aerosol age and the fitting of a linear relationship to the three-year combined data set. Through use of f44, a variable that indicates aerosol age, results indicated that most CCN captured in our collocated data sets are relatively young. A few higher values present in 2016 are likely indicative of older aerosols that have begun descending into the boundary layer, as also suggested by their observed location relative to other data points. Overall, aerosol age is relatively consistent between years, indicating that analysis of all three years combined does not result in three distinct and differently aged air masses (Figure 5.3). Furthermore, fitting a relationship through the combined three-year data set (Figure 5.9) results in relatively high R^2 values, suggesting that relationships between CCN concentration and aerosol optical properties are similar for not only different measured locations, but for different stages of the seasonal burning cycle.

SQ (3) targeted an understanding of the conditions under which HSRL-2 observed optical properties provide good constraints for correlation with CCN concentrations. Through sensitivity testing of RH, SS, and collocation criteria values and thresholds, we have found that these relationships are optimized at low ambient RH conditions and high SS values. This is due to effects of hygroscopicity in humid conditions, as well as the ability for more aerosols (of a given size and chemical composition)

to nucleate at high SS. Furthermore, sensitivity testing related to collocation of the HSRL-2 and CCN data sets suggested that correlation between variables is strongest when using short time windows (less than 40 minutes), a horizontal distance of 2 km (roughly equal to the distance over which HSRL-2 data is aggregated), and a vertical bin size between 45-75 m. CCN autocorrelation provided insight in terms of horizontal variability of CCN and confirmed not only that autocorrelation of CCN is high at 2 km, but that future studies could use much longer horizontal distances with which to collocate if also including an average of HSRL-2 data in the horizontal.

Lastly, SQ (4) addressed the differences in correlation for in situ CCN with remotely sensed HSRL-2 optics compared to in situ CCN and calculated optics. The underlying hypothesis of this question was that stronger correlations would result from using 355 nm coefficients, but observations did not always confirm this hypothesis. The use of both lidar+polarimeter retrieved and in situ size distributions to calculate theoretical backscatter and extinction suggested that fine mode aerosols, which constitute the typical CCN size range, should correlate more strongly with 355 nm coefficients due to the smaller wavelength size. These results demonstrated how the presence of coarse mode aerosols contributes to optics without a corresponding contribution to CCN concentration, the issue inherent in using lidar observations to constrain only fine mode aerosols. Relationships between in situ CCN concentration and total calculated optics suggested that 355 nm should still have shown a stronger correlation than 532 nm coefficients. This discrepancy between theoretical calculations and observations needs to be further investigated in future study.

Overall, preliminary results support the plausibility and reproducibility of using HSRL-2 lidar observables to quantitatively obtain CCN information in biomass burning aerosol dominated air masses. This work demonstrates the advantage to deploying such space-borne lidar instruments and the relevance to estimating CCN concentrations without use of in situ measurements. More widely available CCN concentration data would aid in having the resources to further study and understand aerosol-cloud interactions, ultimately reducing the uncertainty of their contribution to radiative forcing of climate.

Bibliography

Adebiyi, A. A., P. Zuidema, and S. J. Abel, 2015: The convolution of dynamics and moisture with the presence of shortwave absorbing aerosols over the southeast atlantic. *J. Climate*, **28**, 1997–2024.

Aerodyne, 2021: Aerosol mass spectrometer. URL https://www.aerodyne.com/product/aerosol-mass-spectrometer/.

Albrecht, B. A., 1989: Aerosols, cloud microphysics, and fractional cloudiness. *Science*, **245**, 1227–1230.

Anderson, T. L., R. J. Charlson, D. M. Winker, J. A. Ogren, and K. Holmén, 2003: Mesoscale variations of tropospheric aerosols. *J. Atmos. Sci.*, **60**, 119–136.

Andreae, M. O., 2009: Correlation between cloud condensation nuclei concentration and aerosol optical thickness in remote and polluted regions. *Atmos. Chem. Phys.*, **9**, 543–556.

Andreae, M. O., and P. Merlet, 2001: Emission of trace gases and aerosols from biomass burning. *Global Biogeochem. Cycles*, **15**, 955–966.

Andreae, M. O., and D. Rosenfeld, 2008: Aerosol-cloud-precipitation interactions. part 1. the nature and sources of cloud-active aerosols. *Earth-Science Reviews*, **89**, 13–41.

Bellouin, N., and Coauthors, 2020: Radiative forcing of climate change from the copernicus reanalysis of atmospheric composition. *Earth Syst. Sci. Data*, **12**, 1649–1677.

Bony, S., and J.-L. Dufresne, 2005: Marine boundary layer clouds at the heart of tropical cloud feedback uncertainties in climate models. *Geophys. Res. Letters*, **32**, L20 806.

Boucher, O., and Coauthors, 2013: Chapter 7: Clouds and aerosols. *Climate Change 2013: The Physical Science Basis. Contribution of Working Group I to the Fifth Assessment Report of the Intergovernmental Panel on Climate Change*, T. F. Stocker, D. Qin, G.-K. Plattner, M. Tignor, S. K. Allen, J. Boschung, A. Nauels, Y. Xia, V. Bex, and P. M. Midgley, Eds., Vol. 1, Cambridge University Press, chap. 7, 571–657.

Breon, F. M., 2002: Aerosol effect on cloud droplet size monitored from satellite. *Science*, **295**, 834–838.

Buchholz, R. R., and Coauthors, 2021: Air pollution trends measured from terra: Co and aod over industrial, fire-prone, and background regions. *Remote Sensing of Environment*, **256**, 112 275.

Budyko, M. I., 1969: The effect of solar radiation variations on the climate of the earth. *Tellus*, **21**, 611–619.

Burton, S. P., and Coauthors, 2018: Calibration of a high spectral resolution lidar using a michelson interferometer, with data examples from oracles. *Applied Optics*, **57**, 6061–6075.

Che, H., P. Stier, H. Gordon, D. Watson-Parris, and L. Deaconu, 2020: The significant role of biomass burning aerosols in clouds and radiation in the south-eastern atlantic ocean. *Atmos. Chem. Phys.*, **preprint**, 1–27.

DMT, 2017: Ultra high sensitivity aerosol spectrometer (uhsas) operator manual. URL `https://www.dropletmeasurement.com/product`.

Ghan, S. J., and D. R. Collins, 2004: Use of in situ data to test a raman lidar-based cloud condensation nuclei remote sensing method. *J. Atmos. Oceanic Tech.*, **21**, 387–394.

Ghan, S. J., and Coauthors, 2006: Use of in situ cloud condensation nuclei, extinction, and aerosol size distribution measurements to test a method for retrieving cloud condensation nuclei profiles from surface measurements. *J. Geophys. Res.*, **111**, D05S10.

Hair, J. W., and Coauthors, 2008: Airborne high spectral resolution lidar for profiling aerosol optical properties. *Applied Optics*, **47**, 6734–6752.

Haywood, J., and O. Boucher, 2000: Estimates of the direct and indirect radiative forcing due to tropospheric aerosols: A review. *Rev. Geophys.*, **38**, 513–543.

Jeong, M.-J., Z. Li, E. Andrews, and S.-C. Tsay, 2007: Effect of aerosol humid-ification on the column aerosol optical thickness over the atmospheric radiation measurement southern great plains site. *J. Geophys. Res*, **112**, D10 202.

Kacarab, M., and Coauthors, 2020: Biomass burning aerosol as a modulator of droplet number in the southeast atlantic region. *Atmos. Chem. Phys.*, **20**, 3029–3040.

Kapustin, V. N., A. D. Clarke, Y. Shinozuka, S. Howell, V. Brekhovskikh, T. Naka-jima, and A. Higuashi, 2006: On the determination of a cloud condensation nuclei from satellite: Challenges and possibilities. *J. Geophys. Res.*, **111**, D04 202.

Kaufman, Y. J., J. M. Haywood, P. V. Hobbs, W. Hart, R. Kleidman, and B. Schmid, 2003: Remote sensing of vertical distributions of smoke aerosol off the coast of africa. *Geophys. Res. Lett.*, **30**.

Köhler, H., 1936: The nucleus in and the growth of hygroscopic droplets. *Trans. Faraday Soc.*, **32**, 1152–1161.

Lance, S., A. Nenes, J. Medina, and J. N. Smith, 2006: Mapping the operation of the dmt continuous flow ccn counter. *Aerosol Science and Technology*, **40**, 242–254.

Lin, C.-Y., H. m. Hsu, Y. H. Lee, C. H. Kuo, Y.-F. Sheng, and D. A. Chu, 2009: A new transport mechanism of biomass burning from indochina as identified by modeling studies. *Atmos. Chem. Phys.*, **9**, 7901–7911.

Liu, J., Y. Zheng, Z. Li, C. Flynn, and M. Cribb, 2012: Seasonal variations of aerosol optical properties, vertical distribution and associated radiative effects in the yangtze delta region of china. *J. Geophys. Res.*, **117**, D16.

Liu, Y., P. Koutrakis, R. Kahn, S. Turquety, and R. M. Yantosca, 2007: Estimating fine particulate matter component concentrations and size distributions using satellite-retrieved fractional aerosol optical depth: Part 2 - a case study. *Journal of the Air & Waste Management Association*, **57**, 1360–1369.

Lohmann, U., and J. Feichter, 2005: Global indirect aerosol effects: A review. *Atmos. Chem. Phys*, **5**, 715–737.

Lv, M., and Coauthors, 2018: Retrieval of cloud condensation nuclei number concentration profiles from lidar extinction and backscatter data. *J. Geophys. Res: Atmospheres*, **123**, 6082–6098.

Martins, J. V., P. Artaxo, C. Liousse, J. S. Reid, P. V. Hobbs, and Y. J. Kaufman, 1998: Effects of black carbon content, particle size, and mixing on light absorption by aerosols from biomass burning in brazil. *J. Geophys. Res.*, **103**, 32 041–32 050.

Mitchell, J. M., 1971: The effect of atmospheric aerosols on climate with special reference to temperature near the earth's surface. *J. Appl. Meteor. Climatol.*, **10**, 703–714.

Myrhe, G., and Coauthors, 2013: Chapter 8: Anthropogenic and natural radiative forcing. *Climate Change 2013: The Physical Science Basis. Contribution of Working Group I to the Fifth Assessment Report of the Intergovernmental Panel on Climate Change*, T. F. Stocker, D. Qin, G.-K. Plattner, M. Tignor, S. K. Allen, J. Boschung, A. Nauels, Y. Xia, V. Bex, and P. M. Midgley, Eds., Vol. 1, Cambridge University Press, chap. 7, 659–740.

Nam, C., S. Bony, J.-L. Dufresne, and H. Chepfer, 2012: The 'too few, too bright' tropical low-cloud problem in cmip5 models. *Geophys. Res. Letters*, **39**, L21 801.

of the IPCC, W. G. I., 2013: Climate change 2013, the physical science basis: Summary for policymakers, technical summary and frequently asked questions. Tech. rep., Intergovernmental Panel on Climate Change. URL `https://www.ipcc.ch/report/ar5/wg1/`.

Omar, A. H., and Coauthors, 2009: The calipso automated aerosol classification and lidar ratio selection algorithm. *J. Atmos. Oceanic Tech.*, **26**, 1994–2014.

Penner, J. E., and Coauthors, 2001: Chapter 5: Aerosols, their direct and indirect effects. *Climate Change 2001: The Scientific Basis. Contribution of Working Group I to the Third Assessment Report of the Intergovernmental Panel on Climate Change*,

J. T. Houghton, Y. Ding, D. J. Griggs, M. Noguer, P. J. van der Linden, X. Dai, K. Maskell, and C. A. Johnson, Eds., Vol. 1, Cambridge University Press, chap. 5, 291–348.

Petters, M. D., and S. M. Kreidenweis, 2007: A single parameter representation of hygroscopic growth and cloud condensation nucleus activity. *Atmos. Chem. Phys.*, **7**, 1961–1971.

Petty, G. W., 2006: *A First Course in Atmospheric Radiation: Second Edition.* Sundog Publishing.

Prather, K. A., C. D. Hatch, and V. H. Grassian, 2008: Analysis of atmospheric aerosols. *Annual Rev. Anal. Chem.*, **1**, 485–514.

Ramanathan, V., 2001: Aerosols, climate, and the hydrological cycle. *Science*, **294**, 2119–2124.

Redemann, J., and Coauthors, 2021: An overview of the oracles (observations of aerosols above clouds and their interactions) project: aerosol-cloud-radiation interactions in the southeast atlantic basin. *Atmos. Chem. Phys.*, **21**, 1507–1563.

Roberts, G. D., and A. Nenes, 2005: A continuous-flow streamwise thermal-gradient ccn chamber for atmospheric measurements. *Aerosol Science and Technology*, **39**.

Rosenfeld, D., and Coauthors, 2014: Global observations of aerosol-cloud-precipitation-climate interactions. *Rev. Geophys.*, **52**, 750–808.

Ross, K. E., S. J. Piketh, R. T. Bruintjes, R. P. Burger, R. J. Swap, and H. J. Annegarn, 2003: Spatial and seasonal variations in ccn distribution and the aerosol-ccn relationship over southern africa. *J. Geophys. Res.*, **108**, D13.

Shinozuka, Y., and Coauthors, 2009: Aerosol optical properties relevant to regional remote sensing of ccn activity and links to their organic mass fraction: airborne observations over central mexico and the us west coast during milagro/intex-b. *Atmos. Chem. Phys.*, **9**, 6727–6742.

Shinozuka, Y., and Coauthors, 2020: Modeling the smoky troposphere of the southeast atlantic: a comparison to oracles airborne observations from september of 2016. *Atmos. Chem. Phys.*, **20**, 11 491–11 526.

Sotiropoulou, R.-E. P., A. Nenes, P. J. Adams, and J. H. Seinfeld, 2007: Cloud condensation nuclei prediction error from application of köhler theory: Importance for the aerosol indirect effect. *J. Geophys. Res.*, **112**, D12 202.

Stevens, B., and G. Feingold, 2009: Untangling aerosol effects on clouds and precipitation in a buffered system. *Nature*, **461**, 607–613.

TSI, 2017: Aerodynamic particle sizer model 3321 spec sheet. URL https://tsi.com/products/particle-sizers/.

Twomey, S., 1974: Pollution and the planetary albedo. *Atmos. Env.*, **8**, 1251–1256.

Xu, F., and Coauthors, 2021: A combined lidar-polarimeter inversion approach for aerosol remote sensing over ocean. *Front. Remote Sens.*, **2**, 620 871.

Zuidema, P., J. Redemann, J. Haywood, R. Wood, S. Piketh, M. Hipondoka, and P. Formenti, 2016: Smoke and clouds above the southeast atlantic: Upcoming field campaigns probe absorbing aerosol's impact on climate. *Bull. Amer. Meteor. Soc.*, **97**, 1131–1135.